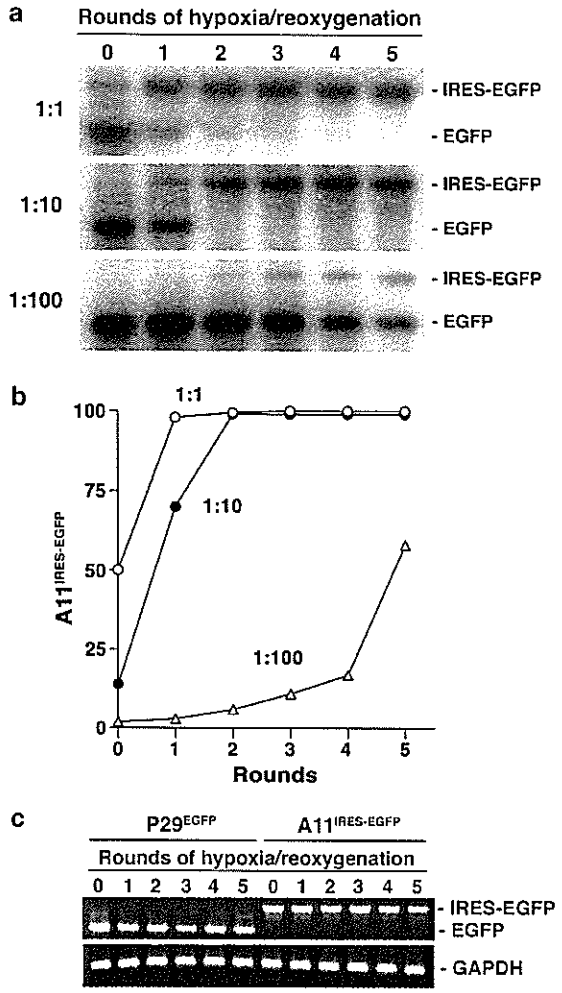

Figure 7 Hypoxia-reoxygenation selects $A11^{IRES\text{-}EGFP}$ cells in a mixed culture. (**a**) Southern blot of PCR fragments amplified using genomic DNA extracted from mixtures of $P29^{EGFP}$ and $A11^{IRES\text{-}EGFP}$ cells. $A11^{IRES\text{-}EGFP}$ were mixed with $P29^{EGFP}$ cells at a 1:1, 1:10 or 1:100 ratio and treated with multiple rounds of hypoxia-reoxygenation. (**b**) Selection of $A11^{IRES\text{-}EGFP}$ cells following hypoxia-reoxygenation treatment. The percentage of $A11^{IRES\text{-}EGFP}$ cells was calculated by the standard curve shown in Figure 6f after measuring the relative intensities of the PCR bands shown in (**a**). The data are representative of two separate experiments in which similar results were obtained. (**c**) Stability of the integrated marker genes in $P29^{EGFP}$ and $A11^{IRES\text{-}EGFP}$ cells. Ethidium bromide staining of the PCR bands is shown.

cells nearly overtook $P29^{EGFP}$ cells only in the local normoxic areas that were dissected by microdissection. The percentage of $A1^{IRES\text{-}EGFP}$ cells was over 50% in #1 and #6 tumors, suggesting that the cells were overtaking $P29^{EGFP}$ cells in these tumors. In other 3 tumors, the percentage was below 50%, indicating that selection of $A11^{IRES\text{-}EGFP}$ cells was occurring in local hypoxic areas of these tumors but was not apparent in whole tumor mass.

Discussion

The data presented here showed a close correlation between metastatic potential and the resistance to hypoxia-induced apoptosis among the cell lines with differing metastatic potential. They also showed that the high-metastatic cells are more resistant to ER stress-induced apoptosis. The hypoxia-induced apoptosis may be p53-independent, because hypoxia neither caused p53 accumulation nor induced the expressions of endogenous downstream p53 effector proteins. An apoptosis-specific expression profiling and immunoblot analyses demonstrated a correlation between the resistance to hypoxia-induced apoptosis and the expression level of Mcl-1. Downregulation of the Mcl-1 expression in A11 cells by Mcl-1 siRNA increased the sensitivity to hypoxia-induced cell death and, importantly, decreased the metastatic ability. Although there are so far few reports directly indicating the involvement of Mcl-1 in metastatic potential of tumor cells, a clinicopathological study suggested Mcl-1 as an indicator of tumor progression and prognosis in patients with gastric carcinoma (Maeta *et al.*, 2004). Therefore, Mcl-1 may be one of the factors that confer metastatic potential on at least some tumor cells.

In agreement with the previous reports (Bruick, 2000; Guo *et al*, 2001), hypoxia induced the expression of Bnip3 in all of the cell lines used in this study. Bnip3 is a mitochondrial protein and induces apoptosis independently of Apaf-1, cytochrome *c* release and caspase activation (Vande Velde *et al.*, 2000). Bcl-2 and Bcl-X_L bind to Bnip3 and inhibit apoptosis caused by the overexpression of Bnip3 (Ray *et al.*, 2000). Therefore, it is possible that Mcl-1 binds to Bnip3 and inhibits Bnip3-induced apoptosis. We preliminarily examined this possibility, and the data showed that Mcl-1 physically interacts with Bnip3 (data not shown).

There was no difference in the inducibility of ER stress- and hypoxia-inducible genes such as GADD153, GRP78 and ORP150 genes between the low- and the high-metastatic cell lines, eliminating the involvement of these genes in the difference of the sensitivity to hypoxia- and ER-stress-induced apoptosis.

The present results clearly demonstrated the survival advantage of A11 cells over P29 cells. In the mixed culture, A11 cells overtook P29 cells during several rounds of hypoxia-reoxygenation. It would be of interest to note that as the rounds of selection proceeded A11 cells progressively became more resistant to apoptosis induced by not only hypoxia but also serum starvation, glucose deprivation and anticancer drugs such as cisplatin and etoposide (not shown). Therefore, it is likely that repeated exposure to hypoxia-reoxygenation results in the selection of not merely A11 cells with original phenotype but of A11 cells with more malignant phenotype, consistent with previous reports (Kim *et al.*, 1997; Kinoshita *et al.*, 2001).

Coinciding with the *in vitro* experiments, the frequency of apoptosis was greater in the hypoxic areas of A11 tumors than in those of P29 tumors. Intriguingly, it appeared that A11 cells became a majority in the hypoxic areas of many tumor masses established from equal mixtures of P29 and A11 cells. It is of note that although we randomly excised the hypoxic areas the proportion of A11 cells in these areas was over 90% in

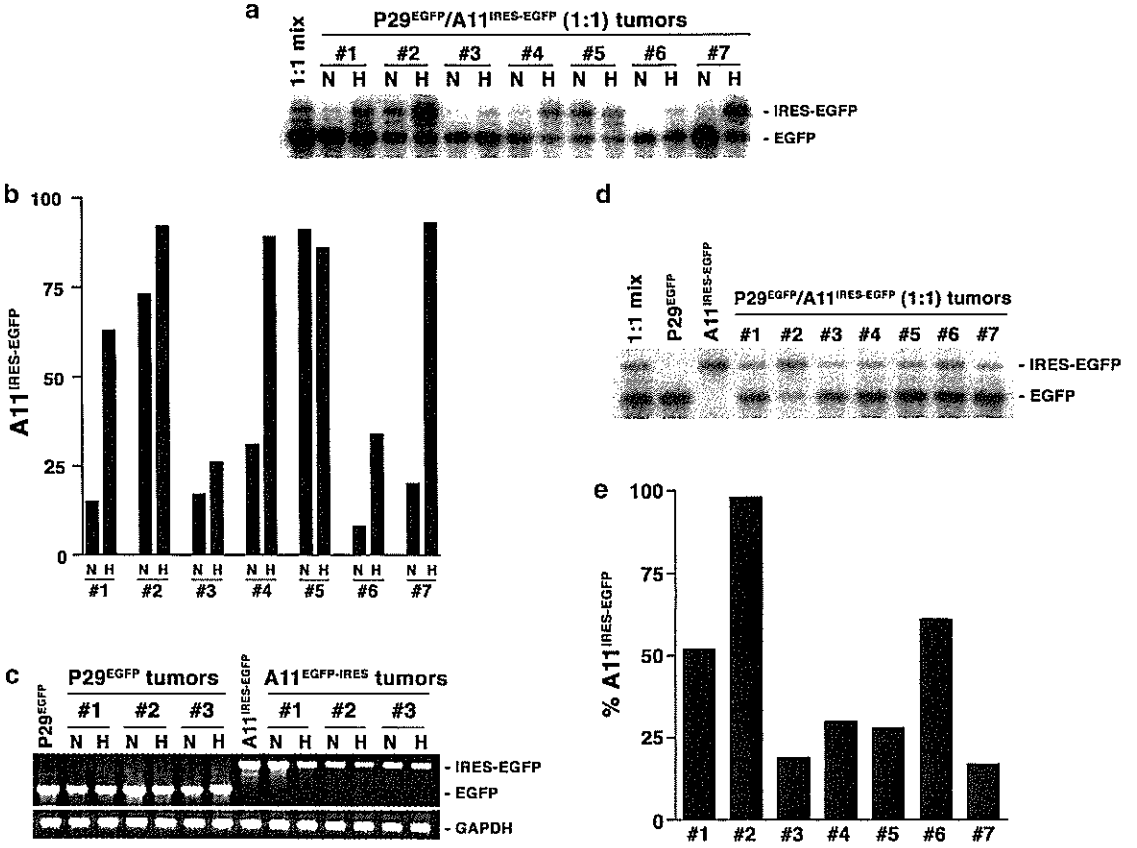

Figure 8 Proportion of A11$^{IRES\text{-}EGFP}$ cells in tumors. (a) Southern blot of PCR fragments amplified using genomic DNA extracted from normoxic (N) and hypoxic (H) areas in subcutaneous tumors established from equal mixtures of P29^{EGFP} and A11$^{IRES\text{-}EGFP}$ cells. (b) The percentage of A11$^{IRES\text{-}EGFP}$ cells in normoxic (N) and hypoxic (H) areas in subcutaneous tumors. The percentage of A11$^{IRES\text{-}EGFP}$ cells was calculated by the standard curve shown in Figure 5f after measuring the relative intensities of the PCR bands shown in (a). (c) Stability of the integrated marker genes in normoxic (N) and hypoxic (H) areas of P29^{EGFP} and A11$^{IRES\text{-}EGFP}$ tumors. Ethidium bromide staining of the PCR bands is shown. (d) Southern blot of PCR fragments amplified using genomic DNA extracted from subcutaneous tumors established from equal mixtures of P29^{EGFP} and A11$^{IRES\text{-}EGFP}$ cells. (e) The percentage of A11$^{IRES\text{-}EGFP}$ cells in subcutaneous tumors. The percentage of A11$^{IRES\text{-}EGFP}$ cells was calculated by the standard curve shown in Figure 6f after measuring the relative intensities of the PCR bands shown in (d). Tumor numbers (#) correspond to those in (a).

several samples. This was somewhat surprising. We had expected that the proportion would vary widely from one sample to another, because the time of hypoxia influences the degree of apoptosis and EF5-binding does not tell us how long hypoxia had lasted in EF5-positive areas before excision. Nevertheless, a majority of P29 cells was commonly lost in the randomly selected hypoxic areas. One possible explanation for this is that P29 cells die more rapidly in *in vivo* hypoxic areas in which starvation of growth factors and nutrients that could act synergistically with hypoxia to induce apoptosis also occurs. We then exposed P29 and A11 cells to serum starvation (0.5% FBS) and hypoxia (0.1% O_2) simultaneously. The data showed that more than 75% of P29 cells died within 24 h while more than 70% of A11 cells survived. Thus, P29 cells are less tolerant towards severer conditions in *in vivo* hypoxic areas than A11 cells, and this might explain the rapid loss of P29 cells in hypoxic areas. Interestingly, we observed two cases out of the seven tumors in which A11 cells dominated in not only hypoxic areas but also normoxic areas. It is possible that the normoxic areas represent the ones that are reoxygenated after hypoxia. Intriguingly, in one case (#2 tumor), the proportion of A11 cells in the tumor mass was over 90%. This suggests that a majority of P29 cells died of apoptosis induced by severe hypoxia and other microenvironmental factors in the early phase of growth of this tumor, resulting in the selection of A11 cells. The degree of tumor vascularization and angiogenesis may vary from one tumor to another even if they are established from the same tumor cells, and accordingly the extent of hypoxia may differ in individual tumor. This may explain the difference in the proportion of A11 cells in each tumor.

It has been reported that hypoxia induces p53-dependent apoptosis and thus selects *p53*$^{-/-}$ cells (Graeber *et al.*, 1996). Our study showed that hypoxia selects for cells with reduced apoptotic potential and high-metastatic ability. This phenomenon could occur in human tumors such as cervical cancer, head and neck cancer and soft tissue sarcoma in which a correlation between hypoxia and aggressiveness or poor prognosis has been reported (Brizel *et al.*, 1996, 1997; Höckel

et al., 1996, 1999). Therefore, the data presented here may have important implications for malignant progression of tumors.

Materials and methods

Cell culture

The cell lines, P29, P34, C2, D6 and A11, established from Lewis lung carcinoma, have been characterized elsewhere (Takasu *et al.*, 1999; Koshikawa *et al.*, 2003). They were grown in Dulbecco's modified Eagle's medium (DMEM) containing 10% fetal bovine serum supplemented with 100 units/ml penicillin and 100 μg/ml streptomycin. Cells were cultured at 37°C in a humidified atmosphere with 5% CO_2 or under hypoxic conditions (ca. 0.1% O_2) generated in BBL GasPak Pouch (Becton Dickinson Microbiology Systems, Cockeysville, MA, USA). In some experiments, they were treated with tunicamycin (Sigma-Aldrich, St Louis, MO, USA), brefeldin A (WAKO Pure Chemical Industries, Ltd., Osaka, Japan), thapsigargin (Sigma-Aldrich), A23187 (Sigma-Aldrich) or vehicle alone.

Assessment of cell viability and apoptosis

Cells were seeded at a concentration of 3×10^5 cells/dish (Falcon 3002), and cell death was induced by culturing them under hypoxic conditions or in the presence of various drugs. For aerobic recovery, the cells were cultured in normoxia until they become subconfluent, thus the recovery time was different for each cell line. Cell viability was assessed by trypan blue dye exclusion. Flow cytometric analysis was performed as described previously (Takasu *et al.*, 1999) to detect cellular DNA fragmentation with a FACScan flow cytometer (Becton Dickinson, Mountain View, CA, USA). Chromatin condensation and fragmentation were visualized by staining the cells with DAPI (10 μg/ml). Annexin V and terminal deoxynucleotidyl transferase-mediated deoxyuridine triphosphate nick-end labeling (TUNEL) stainings were carried out using Annexin V-EGFP Apoptosis Detection Kit (MBL, Nagoya, Japan) and ApopTag Fluorescein *In situ* Apoptosis Detection Kit (Serologicals Corp., Norcross, GA, USA), respectively, according to the manufacturer's instructions. The fluorescence was observed under a Fluoview confocal laser microscope (Olympus, Tokyo, Japan). For clonogenic assay, cells were seeded at a concentration of 100 cells/well of six-well plates (Falcon 3046), incubated for 3 or 4 days under hypoxic (~0.1% O_2) conditions, and then allowed to grow under normoxic conditions for 8–10 days. Colonies were fixed with methanol and stained with 0.05% crystal violet.

Expression profiling of apoptosis-related genes

Expressions of apoptosis-related genes in normoxic and hypoxic P29 and A11 cells were carried out using Mouse Apoptosis GEArray Q™ series containing a panel of 96 key genes involved in apoptosis (SuperArray, Inc., Bethesda, MD, USA). Hybridization of the microarray with a biotin-16-dUTP-labeled cDNA probe and chemiluminescent detection were performed according to the manufacturer's instructions.

Northern blot analysis

Total RNA was electrophoresed on 1% agarose gel containing formaldehyde and transferred to nylon filters. Blots were hybridized with a ^{32}P-labeled mouse *Bnip3* cDNA probe that was prepared by RT–PCR.

Small interfering RNA (siRNA) transfection

Mcl-1 siRNA (Santa Cruz Biotechnologies, Inc., Santa Cruz, CA, USA) or Silencer Negative Control #1 siRNA (Ambion, Inc., Austin, TX, USA) was transfected into A11 cells with Lipofectamine 2000 (Invitrogen, Carlsbad, CA, USA) according to the manufacturer's protocol. At 3 days after transfection, the cells were subjected to immunoblot analysis for Mcl-1 expression, apoptosis assay and metastasis assay.

Immunoblot analysis

Cells were lysed in 1% Triton X-100, 1% sodium deoxycholate, 0.1% SDS, 50 mM Tris-HCl, pH 7.5, 150 mM NaCl, 1 mM PMSF and protease inhibitor cocktail (Sigma-Aldrich) or directly dissolved in SDS sample buffer. After centrifugation at 10 000 *g* for 10 min at 4°C, the supernatant was used for immunoblot analysis. Proteins were separated by SDS–PAGE under reducing conditions and transferred to a nitrocellulose membrane. The membrane was incubated with first antibodies, washed extensively with TBS-T, and then with species-appropriate HRP-conjugated secondary antibodies. The first antibodies used were anti-p53 antibody (Ab-3, Calbiochem-Novabiochem, Germany), anti-Mcl-1 antibody (Santa Cruz Biotechnology, Inc.), anti-GADD153 antibody (Santa Cruz Biotechnology, Inc.), anti-GRP78 antibody (Santa Cruz Biotechnology, Inc.), anti-ORP180 antibody (IBL, Fujioka, Japan) and anti-β-actin antibody (Sigma-Aldrich). Immunodetection was performed using the enhanced chemiluminescence system (ECL; Amersham Biosciences Corp., Piscataway, NJ, USA). The image of the bands was acquired with an imaging densitometer, and the signal intensities were analyzed with an NIH Image 1.63 software on a Machintosh computer. All signals were normalized to β-actin.

Tumor growth and metastasis assays

Cells (2×10^5 cells/mouse) were inoculated into the abdominal flank of age-matched female C57BL/6 mice (Nippon SLC, Hamamatsu, Japan). Subcutaneous tumor growth was monitored by caliper measurement of two diameters at right angles, and the tumor mass was estimated from the equation volume $= 0.5 \times a \times b^2$, where a and b are the larger and smaller diameters, respectively. For spontaneous metastasis assay, the mice were killed 30 days after tumor cell inoculation, and their lungs were removed. For experimental metastasis assay, tumor cells (2×10^5 cells/mouse) were injected intravenously, and the lungs were removed 17 days later. The lungs were fixed in Bouin's solution and the parietal metastatic nodules were counted. All animal experiments were performed in compliance with the institutional guidelines for the care and use of laboratory animals.

Immunohistochemistry

Subcutaneous tumors were excised, fixed in 10% buffered formalin and embedded in paraffin wax. Paraffin sections were cut at 6 μm thickness and mounted on the silane-coated glass slides. After routine dewaxing and rehydrating, the sections were incubated in 1 × ChemMate®Target Retrieval Solution (DakoCytomation, Glostrup, Denmark) at 121°C for 15 min and rinsed with Dulbecco's phosphate-buffered saline (DPBS). For quenching endogenous peroxidase activity, the sections were incubated in 0.3% H_2O_2 in methanol for 30 min. Thereafter, they were incubated with diluted normal goat serum for 20 min at room temperature and then incubated with anti-Mcl-1 antibody or normal rabbit IgG (4 μg/ml) diluted in ChemMate® Antibody Diluent (DaKoCytomation) containing 2% dry milk at 4°C for 16 h. Immunostaining was carried out by using VECTASTAIN® ABC Kit according to the

manufacturer's instructions. The sections were washed with DPBS and finally counterstained with hematoxylin.

Detection and microdissection of hypoxic areas in tumors
In all, 300 μl of EF5 solution (3 mg/ml) was injected intraperitoneally into mice bearing subcutaneous tumors (Inbal *et al.*, 1997). After 1 h, tumors were surgically removed and frozen in OCT compound. Cryostat sections cut at 10 μm were fixed with 4% paraformaldehyde and washed with DPBS. The sections were treated with 5% mouse serum, 20% dry milk and 0.3% Tween 20 in DPBS overnight at 4°C to block nonspecific binding sites. They were rinsed with 0.3% Tween 20 in DPBS and then incubated with Cy3-labeled monoclonal anti-EF5 antibody (ELK3-51) for 4 h at 4°C. After extensive washing with DPBS, tissue samples were observed under a confocal laser microscope or a fluorescence microscope. For detection of apoptotic cells *in vivo*, TUNEL staining was performed followed by EF5 staining. In some experiments, EF5 binding-positive (hypoxic) and adjacent EF5 binding-negative (normoxic) areas in tumor tissues were dissected using a laser-assisted microdissection system (Leica Microsystems, Tokyo, Japan).

Establishment of cells transfected with pEGFP-N1 or pIRES2-EGFP plasmid
P29 and A11 cells were transfected with pEGFP-N1 and pIRES2-EGFP (BD Biosciences Clontech, Tokyo, Japan), respectively, using Lipofectin reagent (Invitrogen, Tokyo, Japan). After selecting the transfected P29 or A11 cells in the presence of 800 μg/ml G418, a clone designated $P29^{EGFP}$ or $A11^{IRES\text{-}EGFP}$, respectively, was established. They were routinely cultured in the presence of 400 μg/ml G418.

DNA isolation, PCR and Southern blotting
Genomic DNA was extracted from $P29^{EGFP}$, $A11^{IRES\text{-}EGFP}$, mixed cells, solid tumors or microdissected sections by conventional method, treated with RNase A (10 μg/ml) and phenol extracted again. PCR was performed using 1–100 ng genomic DNA and *r*Taq DNA polymerase (TOYOBO Biochemicals, Osaka, Japan) on a Perkin Elmer GeneAmp PCR System 9700. The sense primer (P1) was 5′-AAC TCCGCCCCATTGACGC-3′ corresponding to the sequence within the CMV promoter, and the antisense primer (P2) was 5′-ACAAACCACAACTAGAATGCAG-3′ corresponding to the sequence in the SV40polyA signal. These primers were designed to amplify the EGFP sequence in pEGFP-N1 plasmid and the IRES-EGFP sequence in pIRES2-EGFP plasmid, thus yielding 1118 and 1693 bp PCR products, respectively. The PCR conditions were 94°C for 3 min, followed by 20–30 cycles of 94°C for 30 s, 55°C for 30 s and 72°C for 1 min. The resulting PCR products were electrophoresed on 1.2% agarose gels, transferred to nylon membranes and hybridized with a ^{32}P-labeled *EGFP* cDNA. The membranes were washed and radioactive intensity corresponding to the EGFP and IRES-EGFP bands was quantitated using a Fluoro Image Analyzer FLA-5000 (FUJIFILM, Tokyo, Japan). The measured percentage of $A11^{IRES\text{-}EGFP}$ cells was determined by dividing the intensity of the IRES-EGFP band by the total intensity of the EGFP plus IRES-EGFP bands. The actual percentage of $A11^{IRES\text{-}EGFP}$ cells in a mixed culture and in a tumor was determined from a standard curve established from Figure 6f.

Acknowledgements
We thank the National Cancer Institute (CTEP) for providing EF5. This work was supported in part by Grant-in-Aid from the Ministry of Health, Labour, and Welfare for Third Term Comprehensive Control Research for Cancer and from the Ministry of Education, Culture, Sports, Science and Technology.

References

Brizel DM, Scully SP, Harrelson JM, Layfield LJ, Bean JM, Prosnitz LR *et al.* (1996). *Cancer Res* **56**: 941–943.
Brizel DM, Sibley GS, Prosnitz LR, Scher RL, Dewhirst MW. (1997). *Int J Radiat Oncol Biol Phys* **38**: 285–289.
Brown JM, Giaccia AJ. (1998). *Cancer Res* **58**: 1408–1416.
Bruick RK. (2000). *Proc Natl Acad Sci USA* **97**: 9082–9087.
Bufalo DD, Biroccio A, Leonetti C, Zupi G. (1997). *FASEB J* **11**: 947–953.
Cairns RA, Kalliomaki T, Hill RP. (2001). *Cancer Res* **61**: 8903–8908.
Chaplin DJ, Hill SA. (1995). *Br J Cancer* **71**: 1210–1213.
Coquelle A, Toledo F, Stern S, Bieth A, Debatisse M. (1998). *Mol Cell* **2**: 259–265.
Dachs GU, Chaplin DJ. (1998). *Semin Radiat Oncol* **8**: 208–216.
Durand RE, Sham E. (1998). *Int J Radiat Oncol Biol Phys* **42**: 711–715.
Fernandez Y, Espana L, Manas S, Fabra A, Sierra A. (2000). *Cell Death Differ* **7**: 350–359.
Friedman AD. (1996). *Cancer Res* **56**: 3250–3256.
Glinsky GV. (1997). *Crit Rev Oncol Hematol* **25**: 175–186.
Glinsky GV, Glinsky VV. (1996). *Cancer Lett* **101**: 43–51.
Graeber TG, Osmanian C, Jacks T, Housman DE, Koch CJ, Lowe SW *et al.* (1996). *Nature* **379**: 88–91.
Graham CH, Forsdike J, Fitzgerald CJ, Macdonald-Goodfellow S. (1999). *Int J Cancer* **80**: 617–623.
Guo K, Searfoss G, Krolikowski D, Pagnoni M, Franks C, Clark K *et al.* (2001). *Cell Death Differ* **8**: 367–376.
Harris AL. (2002). *Nat Rev* **2**: 38–47.
Hill RP. (1990). *Cancer Metastasis Rev* **9**: 137–147.
Höckel M, Schlenger K, Aral B, Mitze M, Schaffer U, Vaupel P. (1996). *Cancer Res* **56**: 4509–4515.
Höckel M, Schlenger K, Höckel S, Vaupel P. (1999). *Cancer Res* **59**: 4525–4528.
Inbal B, Cohen O, Polak-Charcon S, Kopolovic J, Vadai E, Eisenbach L *et al.* (1997). *Nature* **390**: 180–184.
Kim CY, Tsai MH, Osmanian C, Graeber TG, Lee JE, Giffard RG *et al.* (1997). *Cancer Res* **57**: 4200–4204.
Kinoshita M, Johnson DL, Shatney CH, Lee YL, Mochizuki H. (2001). *Int J Cancer* **91**: 322–326.
Koshikawa N, Iyozumi A, Gassmann M, Takenaga K. (2003). *Oncogene* **22**: 6717–6724.
Kuwabara K, Matsumoto M, Ikeda J, Hori O, Ogawa S, Maeda Y *et al.* (1996). *J Biol Chem* **271**: 5025–5032.
Lord EM, Harwell L, Koch CJ. (1993). *Cancer Res* **53**: 5721–5726.
Lowe SW, Lin AW. (2000). *Carcinogenesis* **21**: 485–495.
Maeta Y, Tsujitani S, Matsumoto S, Yamaguchi K, Tatebe S, Kondo A *et al.* (2004). *Gastric Cancer* **7**: 78–84.
McConkey DJ, Greene G, Pettaway CA. (1996). *Cancer Res* **56**: 5594–5599.
Munro S, Pelham HR. (1986). *Cell* **46**: 291–300.

Piret JP, Minet E, Cosse JP, Ninane N, Debacq C, Raes M *et al.* (2005). *J Biol Chem* **280**: 9336–9344.
Ray R, Chen G, Vande Velde C, Cizeau J, Park JH, Reed JC *et al.* (2000). *J Biol Chem* **275**: 1439–1448.
Rice GC, Hoy C, Schimke RT. (1986). *Proc Natl Acad Sci USA* **83**: 5978–5982.
Russo CA, Weber TK, Volpe CM, Stoler DL, Petrelli NJ, Rodriguez-Bigas M *et al.* (1995). *Cancer Res* **55**: 1122–1128.
Semenza GL. (2000). *Crit Rev Biochem Mol Biol* **35**: 71–103.
Semenza GL. (2002). *Trends Mol Med* **8**: S62–S67.
Shtivelman E. (1997). *Oncogene* **14**: 2167–2173.
Takaoka A, Adachi M, Okuda H, Sato S, Yawata A, Hinoda Y *et al.* (1997). *Oncogene* **14**: 2871–2977.
Takasu M, Tada Y, Wang JO, Tagawa M, Takenaga K. (1999). *Clin Exp Metastasis* **17**: 409–416.
Teicher BA. (1994). *Cancer Metastasis Rev* **13**: 139–168.
Vande Velde C, Cizeau J, Dubik D, Alimonti J, Brown T, Israels S *et al.* (2000). *Mol Cell Biol* **20**: 5454–5468.
Wong CW, Lee A, Shientag L, Yu J, Dong Y, Kao G *et al.* (2001). *Cancer Res* **61**: 333–338.
Young SD, Hill RP. (1990). *J Natl Cancer Inst* **82**: 371–380.

FEBS Letters 580 (2006) 627–632

High expression of *N*-acetylglucosaminyltransferase V in favorable neuroblastomas: Involvement of its effect on apoptosis

Kei-ichiro Inamori[a], Jianguo Gu[a,*], Miki Ohira[b], Atsushi Kawasaki[b], Yohko Nakamura[b], Takatoshi Nakagawa[c], Akihiro Kondo[c], Eiji Miyoshi[a], Akira Nakagawara[b], Naoyuki Taniguchi[a]

[a] *Department of Biochemistry, Osaka University Graduate School of Medicine, 2-2 Yamadaoka, Suita, Osaka 565-0871, Japan*
[b] *Division of Biochemistry, Chiba Cancer Center Research Institute, 666-2 Nitona, Chuoh-ku, Chiba 260-8717, Japan*
[c] *Department of Glycotherapeutics, Osaka University Graduate School of Medicine, 2-2 Yamadaoka, Suita, Osaka 565-0871, Japan*

Received 1 December 2005; revised 27 December 2005; accepted 29 December 2005

Available online 5 January 2006

Edited by Laszlo Nagy

Abstract **Neuroblastoma (NBL), derived from the sympathetic precursor cells, is one of the most common pediatric solid tumors. The expression of *N*-acetylglucosaminyltransferase V and IX (GnT-V and GnT-IX) mRNA in 126 primary NBLs were quantitatively analyzed and higher expression levels of GnT-V were found to be associated with favorable stages (1, 2 and 4s). Conversely, the downregulation of GnT-V expression by small interfering RNA resulted in a decrease in the susceptibility to cell apoptosis induced by retinoic acid in NBL cells accompanied by morphological change. These results suggest that GnT-V is associated with prognosis by modulating the sensitivity of NBLs to apoptosis.**

Keywords: Neuroblastoma; GnT-V; GnT-IX; Retinoic acid; Apoptosis

1. Introduction

Aberrant glycosylation occurs in nearly all types of cancers, and has been implicated in the malignancy that is characteristic of the disease [1]. *N*-acetylglucosaminyltransferase V (GnT-V) is one of the most relevant glycosyltransferases to tumor invasion and metastasis, and catalyzes the formation of β1,6GlcNAc branching on *N*-glycans, which is closely associated with malignant transformations [2–6]. Recently, our group and Pierce's group independently reported on a new *N*-acetylglucosaminyltransferase IX (GnT-IX, also referred to as GnT-VB), a GnT-V homolog, that is specifically expressed in the brain [7,8]. GnT-IX transcripts are exclusively expressed in the brain and testis, while GnT-V is expressed ubiquitously in human and mouse tissues. Since both glycosyltransferases are expressed in the mouse brain in a region-specific manner (unpublished data), it is possible that they may have discrete biological functions in the brain. On the other hand, GnT-V and GnT-IX are both highly expressed in both the adult and fetal brain [7,9], as well as in several human neuroblastoma (NBL) cell lines (this study and unpublished data). This prompted us to examine the expression of GnT-V and GnT-IX in primary NBL tissues.

NBL is a tumor derived from primitive cells of the sympathetic nervous system and is the most common solid tumor in childhood [10]. Interestingly, most NBLs in infants regress spontaneously or mature into a benign ganglioneuroma. These tumors usually express high levels of TrkA, and as a result, have a tendency to either undergo apoptosis or differentiation, depending on whether nerve growth factor is present or absent in their microenvironment. On the other hand, in most patients over 1 year of age who have metastatic disease, the tumor grows aggressively and their prognosis is usually poor.

In this study, we carried out a quantitative analysis of the gene expression of these glycosyltransferases by real-time PCR, and the findings indicate that a higher expression of GnT-V is correlated with a favorable prognosis for NBL patients. Furthermore, to explore the underlying molecular mechanism, we devised a knockdown approach, in which small interfering RNA (siRNA)-directed against GnT-V mRNA was used to investigate the susceptibility to cell apoptosis induced by retinoic acid in NBL cells. The results clearly showed that the expression levels of GnT-V are associated with a favorable prognosis, possibly through sensitizing to apoptotic signals.

2. Materials and methods

2.1. RNA isolation from primary NBLs

Fresh, frozen tumor tissues were sent to the Division of Biochemistry, Chiba Cancer Center Research Institute, from various hospitals in Japan with informed consent from the patients' parents. All samples were obtained by surgery or biopsy and had been stored at 80 °C. The RNA samples obtained from 126 patients with NBL were subjected to semiquantitative and quantitative real-time reverse transcription-PCR (RT-PCR) analyses. All of the patients were diagnosed clinically as well as pathologically and were tested for DNA ploidy, MYCN amplification, and TrkA expression. The tumors were staged according to the criteria of the International Neuroblastoma Staging System [11].

2.2. Semiquantitative RT-PCR analysis of primary NBLs

The preparation of total RNA from NBL tissues and the synthesis of the first-strand cDNA were performed as described previously [12]. The cDNA was diluted to a 1:20 solution and then amplified in a final

*Corresponding author. Fax: +81 6 6879 3429.
E-mail address: jgu@biochem.med.osaka-u.ac.jp (J. Gu).

Abbreviations: NBL, neuroblastoma; GnT-V, *N*-acetylglucosaminyltransferase V; GnT-IX, *N*-acetylglucosaminyltransferase IX; RT, reverse transcription; PARP, poly(ADP-ribose) polymerase

0014-5793/$32.00
doi:10.1016/j.febslet.2005.12.089

volume of 10 μl of reaction mixture containing 200 μM of dNTPs, 1× PCR buffer, 0.5 μM of each primer and 0.2 U of rTaq DNA polymerase (Takara Bio, Ohtsu, Japan). The following primer sets were used: GnT-V, 5′-GACCTGCAGTTCCTTCTTCG-3′ and 5′-CCATGGCAGAAGTCCTGTTT-3′; GnT-IX, 5′-CATGGCACCGTGTACTAC-3′ and 5′-TCTGGAGCTCTGCAGAAG-3′. PCR templates were standardized by their GAPDH expression before performing the RT-PCR experiments.

2.3. Quantitative real-time PCR analysis of primary NBLs

2 μl of cDNA prepared as above, either a 100-fold dilution for GnT-V or a 20-fold dilution for GnT-IX, was amplified in a volume of 20 μl with Assay-on-Demand Gene Expression Products (Applied Biosystems) consisting of primers and a TaqMan probe (Assay ID: GnT-V, Hs00159136_m1; GnT-IX, Hs01586304_g1). The thermal cycling conditions and the normalization of the data using GAPDH expression were performed as described previously [12]. All experiments were carried out in triplicate for each data point.

2.4. Assay of GlcNAc transferase activity

The activities of GnT-V and GnT-III in whole cell lysates or microsomal fractions were determined using a pyridylaminated biantennary sugar chain as an acceptor substrate, as described previously [7,13].

2.5. Construction of siRNA vector and retroviral infection

Small interfering oligonucleotides specific for GnT-V were designed on the Takara Bio website (http://www.takara-bio.co.jp/) and the oligonucleotide sequences used in the construction of the siRNA vector were as follows: 5′-GATCCGTTCATTGGCGGAAATTCGTTTCAAGAGAACGAATTTCCGCCAATGAACTTTTTTAT-3′ and 5′-CGATAAAAAAGTTCATTGGCGGAAATTCGTTCTCTTGAAACGAATTTCCGCCAATGAACG-3′. The oligonucleotides were annealed and then ligated into *BamHI*/*ClaI* sites of the pSINsi-hU6 vector (Takara Bio). A retroviral supernatant was obtained by transfection of human embryonic kidney 293 cells using a Retrovirus Packaging Kit Ampho (Takara Bio) according to the manufacturer's protocol. CHP134 cells, a human NBL cell line, were infected with the viral supernatant, and the cells were then selected with 0.5 mg/ml G418 for 2–3 weeks. Stable GnT-V-knockdown clones were selected and confirmed by GnT-V activity and gene expression. Quantitative real-time PCR analyses of GnT-V mRNA expression in these clones were performed with a Smart Cycler II System and the SYBR premix Taq (Takara Bio). RT was carried out at 42 °C for 10 min, followed by 95 °C for 2 min using random primers, followed by PCR for 50 cycles at 95 °C for 5 s and 60 °C for 20 s with the following primers: 5′-AAGCAGGTGTGCCAGGAGAG-3′ and 5′-GTCAAAGGAGGGCACCAGGA-3′. Normalization of the data was performed using the GAPDH mRNA levels.

2.6. Analysis of retinoic acid-induced apoptosis

Parent, mock, and GnT-V-knockdown CHP134 cells were plated on 10 cm culture dishes at 5×10^5 cells in RPMI1640 supplemented with 10% fetal bovine serum, 100 U/ml penicillin, and 0.1 mg/ml streptomycin. After incubation for 24 h, the conditioned media were changed with fresh medium containing various concentrations of all-*trans* retinoic acid (Sigma). The cells were washed twice with PBS and harvested at the indicated times. Retinoic acid-induced apoptosis was estimated by detecting the cleavage of poly ADP-ribose polymerase (PARP) in whole cell lysates by Western blot analysis using a human specific anti-cleaved PARP (Asp214) antibody (Cell Signaling Technology). As a loading control, anti-ERK1/2 (p44/42 MAP Kinase Antibody, Cell Signaling Technology) was used.

2.7. Viability assay of retinoic acid-treated cells

The parent, mock, and GnT-V-knockdown CHP134 cells were seeded on a 96-well plate at 3×10^3 cells/well for 24 h prior to the retinoic acid treatment. The cells were then incubated with or without retinoic acid at the indicated concentrations for 3 days. Cell viability was assayed using a Cell Counting Kit-8 (Dojindo, Kumamoto, Japan) according to the manufacture's instructions. All experiments were carried out in triplicate for each data point.

3. Results

3.1. Association between higher expression levels of GnT-V mRNA and favorable prognosis in primary NBLs

To assess the association between GnT-V or GnT-IX mRNA expression and the prognosis of the NBLs, we first performed semiquantitative RT-PCR analyses using 16 favorable and 16 unfavorable NBLs. As shown in Fig. 1, GnT-V was preferentially expressed in most of the favorable NBLs, while no obvious difference in GnT-IX expression was found between favorable and unfavorable NBLs. Table 1 shows quantitative data for GnT-V and GnT-IX mRNA in 126 primary NBLs with tumor stages (1, 2, 4s versus 3, 4). GnT-V expression was significantly increased in NBLs at favorable stages ($P = 0.021$), and was correlated well with higher expression of TrkA ($P = 0.010$). On the other hand, GnT-IX expression was marginally associated with the stages.

3.2. GnT-V activities in various human NBL cell lines

To determine whether the expression level of GnT-V is also increased in NBL cells, the activities of GnT-V in various human NBL cell lines were examined. As shown in Fig. 2A, each cell line expressed GnT-V activity at distinct levels. The CHP134 cells showed the highest GnT-V activity among the 10 NBL cell lines used in this study. It is known that the cell line is highly sensitive to the induction of apoptosis by all-*trans* retinoic acid [14,15]. In fact, it is thought that favorable NBLs usually express higher levels of TrkA, and tend to regress spontaneously due to apoptosis. As shown in Fig. 2B, in CHP134 cells that had been treated with retinoic acid at a concentration of 1 μM or 5 μM, PARP cleavage, a marker for apoptosis, occurred, which is one of the main cleavage targets of caspase-3

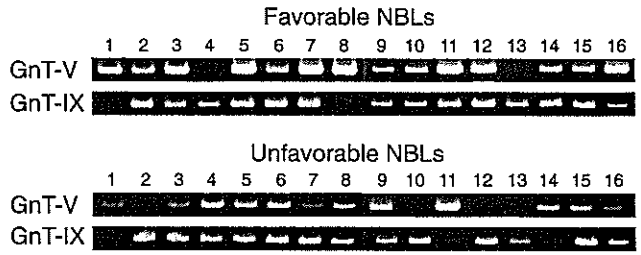

Fig. 1. Semiquantitative RT-PCR analysis of favorable and unfavorable subsets of NBL. Sixteen favorable cases were in stage 1 with no MYCN amplification and a high TrkA expression, while 16 unfavorable cases were in stage 3 or 4 with MYCN amplification and a low TrkA expression.

Table 1
Association of tumor stages and *TrkA* expression in NBL patients with GnT-V or GnT-IX mRNA expression levels

	n	GnT-V[a]	*P*	GnT-IX[a]	*P*
Tumor stage					
1, 2, 4s	57	2.23 ± 0.29	0.021	1.78 ± 0.25	0.21
3, 4	69	1.48 ± 0.16		2.23 ± 0.25	
TrkA expression					
High	59	2.11 ± 0.27	0.010	1.86 ± 0.17	0.75
Low	48	1.33 ± 0.13		1.98 ± 0.34	

[a]Means ± S.E.M.

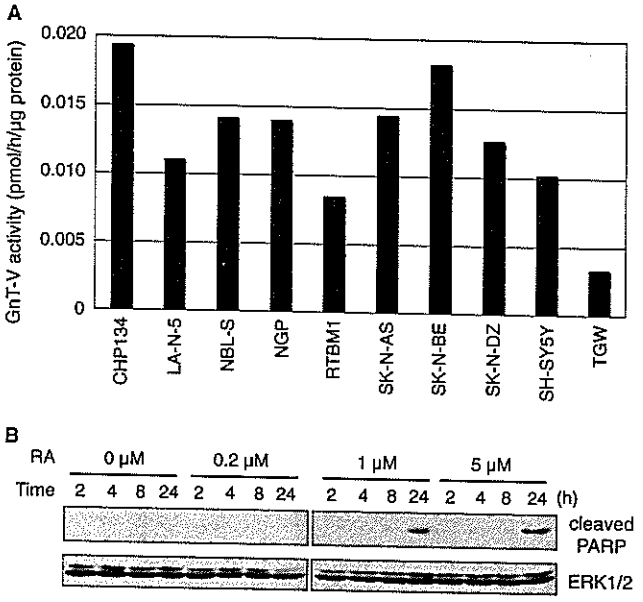

Fig. 2. GnT-V activities in various NBL cell lines and retinoic acid-induced apoptosis of CHP134 cells. (A) GnT-V activity of each of the NBL cells was measured using a whole cell lysate as an enzyme source. (B) Western blot of whole cell lysate of CHP134 cells. Cell apoptosis was observed by staining of cleaved PARP after treatment of retinoic acid (RA) at indicated concentrations and times. The expression levels of ERK1/2 were confirmed as a loading control.

in vivo [16,17]. Thus, we chose this cell line for further analysis of the effects of GnT-V on apoptosis.

3.3. Knockdown of GnT-V expression in CHP134 cells

We prepared a retroviral siRNA vector containing a small hairpin construct capable of generating a duplex RNAi oligonucleotide corresponding to human GnT-V. After retroviral infection, CHP134 cells were selected based on their resistance to G418, and clones with decreased GnT-V activities were chosen. The GnT-V activities were effectively downregulated by 80%, compared with those in parent or mock cells (Fig. 3A), while GnT-III activity, as a control, showed no significant changes between those cells. A quantitative real-time PCR analysis also indicated the downregulation of RNAi-directed GnT-V mRNA expression in these cells (Fig. 3B). It is noteworthy that the cells in GnT-V-knockdown clones showed more spreading on the culture dishes, rather than the spindle shapes of the parent and mock cells (Fig. 4), suggesting that GnT-V may affect cellular cytoskeletal formation. In fact, Guo et al. reported that the overexpression of GnT-V in human HT1080 cells resulted in a decrease in cell adhesion on fibronectin [18].

3.4. Decreased susceptibility to retinoic acid-induced apoptosis in GnT-V-knockdown cells

To evaluate the effects of GnT-V expression on susceptibility to apoptosis induction in CHP134 cells, we examined cell viabilities in the presence of retinoic acid. After treatment with different concentrations of retinoic acid, we found that GnT-V-knockdown cells (KD1 and KD2 in Fig. 5A) had a tendency to be resistant to stimulation by retinoic acid. We further assessed the apoptosis level in retinoic acid-treated cells by PARP cleavage. The GnT-V-knockdown cells showed dramatically reduced levels of PARP cleavage (Fig. 5B). Collectively, these results suggest that GnT-V may sensitize cells to apoptotic signals, which partly contribute to the favorable prognosis of NBL.

4. Discussion

Previous studies demonstrated that an increased amount of β1,6-branched oligosaccharides, formed by the action of GnT-V, are correlated with metastatic potential [2], and this has been shown to be a marker of tumor progression in human breast and colon neoplasia [19], and a prognostic marker in human colorectal carcinoma [20,21]. However, it is not always the case, as evidenced by the fact that Dosaka-Akita et al. reported that the lower expression of GnT-V is associated with a shorter survival and a poor prognosis in non-small cell lung cancers [22]. The present study also suggested that a higher expression of GnT-V is related to a favorable prognosis in NBLs.

GnT-V and GnT-IX, two closely related glycosyltransferases, are expressed in both the adult and fetal brain [7,9]. GnT-V expression is upregulated in E9.5 embryos, and is then

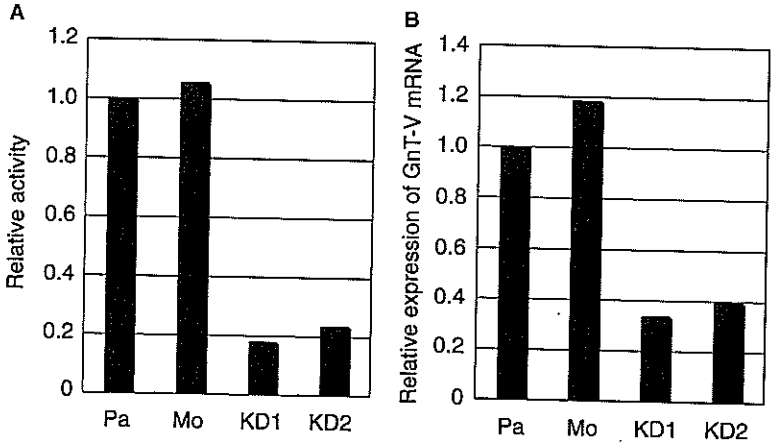

Fig. 3. Enzyme activities and mRNA expression levels in siRNA-mediated GnT-V-knockdown cells. (A) GnT-V activities of GnT-V-knockdown CHP134 cells. The microsomal fraction was used as an enzyme source in the assay. (B) mRNA expression of GnT-V in knockdown cells. Quantitative analysis was performed by real-time PCR. Pa, parent cells; Mo, mock cells; KD1 and KD2, GnT-V-knockdown cells.

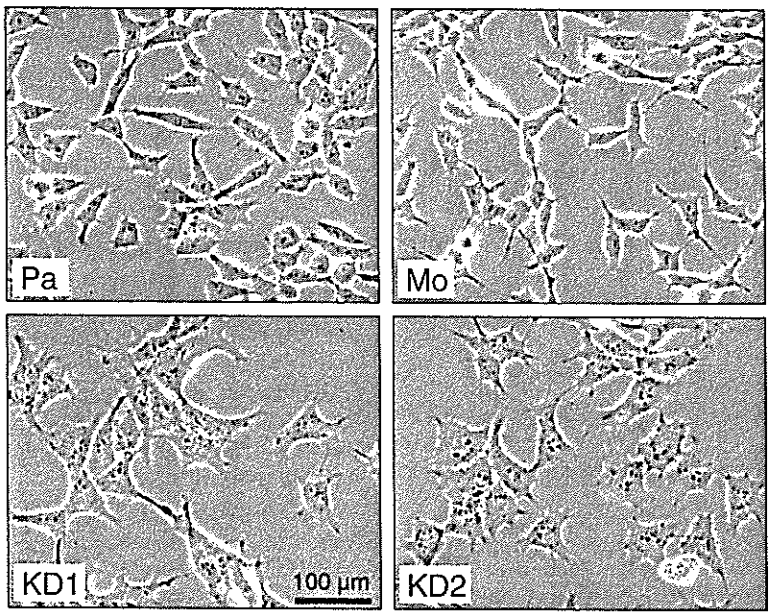

Fig. 4. Morphological changes in GnT-V-knockdown cells. Parent (Pa), mock (Mo), and GnT-V-knockdown CHP134 cells (KD1, KD2) were plated on culture dishes and incubated for 24 h in culture media. Cell shapes were observed by phase contrast microscopy.

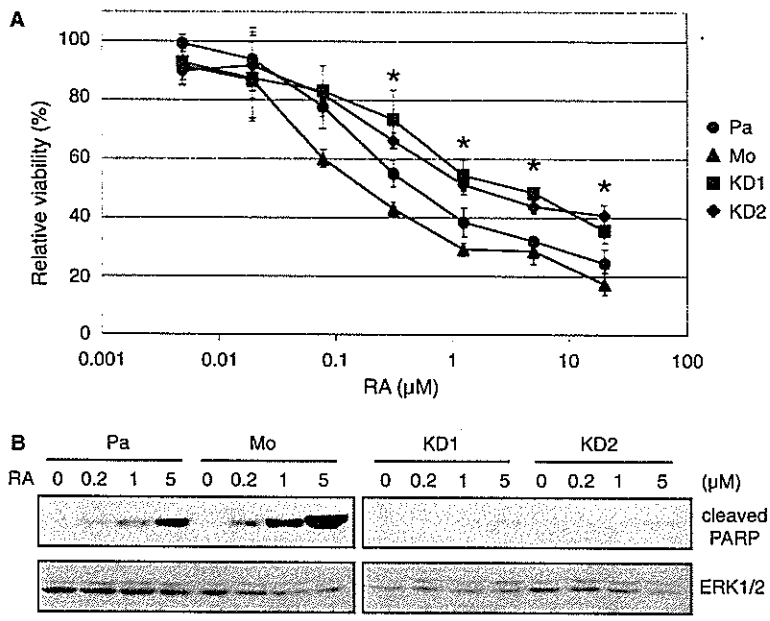

Fig. 5. Cell viabilities and PARP cleavage in retinoic acid-treated GnT-V-knockdown cells. Cell viabilities of parent (Pa), mock (Mo), and GnT-V-knockdown cells (KD1, KD2) were performed as described in Section 2 (A). Cells were treated with retinoic acid at the indicated concentrations for 3 days. $^{*}P < 0.05$. (B) Western blot of cleaved PARP in a cell lysate using an anti-cleaved PARP antibody. Cells were harvested for analysis 24 h after retinoic acid-treatment.

restricted to regions comprised of several specialized epithelial cell layers and the neuroepithelium of the developing central nervous system [9]. On the other hand, GnT-IX is dominantly expressed in the human and mouse brain [7,23]. Thus, we attempted to examine the expressions of GnT-V and GnT-IX in primary NBL tissues.

The frequent gain of the chromosome 17q has been reported to be associated with a poor prognosis [24], and the preferential gain of the region from 17q22-qter indicated a dosage effect that provides a selective advantage to be aggressive NBLs [25]. The gene responsible for the selective advantage is unknown, but a candidate gene that is a member of the inhibitor of apoptosis proteins, survivin, which is mapped to 17q25, has been reported [14]. Although the GnT-IX gene is also mapped to 17q25 [7], an unequivocal correlation with prognosis was not observed in this study. Interestingly, a significant association between expression levels of GnT-V mRNA and the prognosis of 126 NBL patients was observed by real-time PCR analysis. Several human NBL cell lines also consistently express GnT-V. To understand the molecular mechanism associated with the

higher expression levels of GnT-V in the favorable prognosis of NBLs, we selected CHP134 cells as a cell model. Since the cell line is highly sensitive to retinoic acid-induced apoptosis [14,15], we compared the effects of retinoic acid on apoptosis between parent cells and GnT-V-knockdown cells.

In fact, GnT-V-knockdown cells showed a tendency to escape from retinoic acid-induced apoptosis, as confirmed by a cell viability assay and the extent of cleaved PARP, supporting the notion that a higher expression of GnT-V is correlated with a favorable prognosis of NBLs. It is noteworthy that a prominent morphological alteration with increased spreading was observed in the GnT-V-knockdown cells. The altered characteristic of GnT-V-knockdown CHP134 cells observed in this study is consistent with those of previous studies [3,18,26,27]. The overexpression of GnT-V enhances the metastatic potential in several cell types with reduced cell-matrix adhesion and increased motility [3,18,26]. Furthermore, GnT-V expression in human glioma cell line U-373 MG sensitizes these cells to drag-induced apoptosis [28]. Conversely, GnT-V null mouse embryonic fibroblasts exhibited an enhanced adhesion and spreading with associated reduced cell migration [27]. In addition, no significant effect of GnT-V overexpression was observed on apoptotic behavior in fibrosarcoma HT1080 cells, a fibroblast cell line, but a similar phenotypic change with regard to adhesion and migration has been reported [18]. In general, the adhesion of epithelial cells to extracellular matrices is weaker than that of fibroblast cells, and such adhesion is thought to be synergized with the signals of growth factor receptors for modulating cell proliferation and apoptosis. Therefore, we speculate that the GnT-V-induced decrease in cell adhesion could be a plausible factor responsible for the favorable prognosis in NBLs.

In conclusion, a correlation between higher expression levels of GnT-V with a favorable prognosis of NBL patients was found, and GnT-V may cause these tumors to regress by increasing their susceptibility to apoptosis.

Acknowledgments: This work was supported a Grant-in-Aid for Scientific Research (S) No. 13854010 from the Japan Society for the promotion of Science and by the 21st Century COE Program by the Ministry of Education, Science, Culture, Sports and Technology in Japan.

References

[1] Hakomori, S. (2002) Glycosylation defining cancer malignancy: new wine in an old bottle. Proc. Natl. Acad. Sci. USA 99, 10231–10233.

[2] Dennis, J.W., Laferte, S., Waghorne, C., Breitman, M.L. and Kerbel, R.S. (1987) Beta 1–6 branching of Asn-linked oligosaccharides is directly associated with metastasis. Science 236, 582–585.

[3] Demetriou, M., Nabi, I.R., Coppolino, M., Dedhar, S. and Dennis, J.W. (1995) Reduced contact-inhibition and substratum adhesion in epithelial cells expressing GlcNAc-transferase V. J. Cell. Biol. 130, 383–392.

[4] Granovsky, M., Fata, J., Pawling, J., Muller, W.J., Khokha, R. and Dennis, J.W. (2000) Suppression of tumor growth and metastasis in Mgat5-deficient mice. Nat. Med. 6, 306–312.

[5] Saito, T., Miyoshi, E., Sasai, K., Nakano, N., Eguchi, H., Honke, K. and Taniguchi, N. (2002) A secreted type of beta 1,6-*N*-acetylglucosaminyltransferase V (GnT-V) induces tumor angiogenesis without mediation of glycosylation: a novel function of GnT-V distinct from the original glycosyltransferase activity. J. Biol. Chem. 277, 17002–17008.

[6] Ihara, S., Miyoshi, E., Ko, J.H., Murata, K., Nakahara, S., Honke, K., Dickson, R.B., Lin, C.Y. and Taniguchi, N. (2002) Prometastatic effect of *N*-acetylglucosaminyltransferase V is due to modification and stabilization of active matriptase by adding beta 1–6 GlcNAc branching. J. Biol. Chem. 277, 16960–16967.

[7] Inamori, K., Endo, T., Ide, Y., Fujii, S., Gu, J., Honke, K. and Taniguchi, N. (2003) Molecular cloning and characterization of human GnT-IX, a novel {beta}1,6-*N*-acetylglucosaminyltransferase that is specifically expressed in the brain. J. Biol. Chem. 278, 43102–43109.

[8] Kaneko, M., Alvarez-Manilla, G., Kamar, M., Lee, I., Lee, J.K., Troupe, K., Zhang, W., Osawa, M. and Pierce, M. (2003) A novel beta(1,6)-*N*-acetylglucosaminyltransferase V (GnT-VB). FEBS Lett. 554, 515–519.

[9] Granovsky, M., Fode, C., Warren, C.E., Campbell, R.M., Marth, J.D., Pierce, M., Fregien, N. and Dennis, J.W. (1995) GlcNAc-transferase V and core 2 GlcNAc-transferase expression in the developing mouse embryo. Glycobiology 5, 797–806.

[10] Brodeur, G.M. (2003) Neuroblastoma: biological insights into a clinical enigma. Nat. Rev. Cancer 3, 203–216.

[11] Brodeur, G.M., Pritchard, J., Berthold, F., Carlsen, N.L., Castel, V., Castelberry, R.P., De Bernardi, B., Evans, A.E., Favrot, M. and Hedborg, F., et al. (1993) Revisions of the international criteria for neuroblastoma diagnosis, staging, and response to treatment. J. Clin. Oncol. 11, 1466–1477.

[12] Kato, C., Miyazaki, K., Nakagawa, A., Ohira, M., Nakamura, Y., Ozaki, T., Imai, T. and Nakagawara, A. (2004) Low expression of human tubulin tyrosine ligase and suppressed tubulin tyrosination/detyrosination cycle are associated with impaired neuronal differentiation in neuroblastomas with poor prognosis. Int. J. Cancer 112, 365–375.

[13] Taniguchi, N., Nishikawa, A., Fujii, S. and Gu, J.G. (1989) Glycosyltransferase assays using pyridylaminated acceptors: *N*-acetylglucosaminyltransferase III, IV, and V. Meth. Enzymol. 179, 397–408.

[14] Islam, A., Kageyama, H., Takada, N., Kawamoto, T., Takayasu, H., Isogai, E., Ohira, M., Hashizume, K., Kobayashi, H., Kaneko, Y. and Nakagawara, A. (2000) High expression of Survivin, mapped to 17q25, is significantly associated with poor prognostic factors and promotes cell survival in human neuroblastoma. Oncogene 19, 617–623.

[15] Takada, N., Isogai, E., Kawamoto, T., Nakanishi, H., Todo, S. and Nakagawara, A. (2001) Retinoic acid-induced apoptosis of the CHP134 neuroblastoma cell line is associated with nuclear accumulation of p53 and is rescued by the GDNF/Ret signal. Med. Pediatr. Oncol. 36, 122–126.

[16] Nicholson, D.W., Ali, A., Thornberry, N.A., Vaillancourt, J.P., Ding, C.K., Gallant, M., Gareau, Y., Griffin, P.R., Labelle, M. and Lazebnik, Y.A., et al. (1995) Identification and inhibition of the ICE/CED-3 protease necessary for mammalian apoptosis. Nature 376, 37–43.

[17] Tewari, M., Quan, L.T., O'Rourke, K., Desnoyers, S., Zeng, Z., Beidler, D.R., Poirier, G.G., Salvesen, G.S. and Dixit, V.M. (1995) Yama/CPP32 beta, a mammalian homolog of CED-3, is a CrmA-inhibitable protease that cleaves the death substrate poly(ADP-ribose) polymerase. Cell 81, 801–809.

[18] Guo, H.B., Lee, I., Kamar, M., Akiyama, S.K. and Pierce, M. (2002) Aberrant *N*-glycosylation of beta1 integrin causes reduced alpha5beta1 integrin clustering and stimulates cell migration. Cancer Res. 62, 6837–6845.

[19] Fernandes, B., Sagman, U., Auger, M., Demetrio, M. and Dennis, J.W. (1991) Beta 1–6 branched oligosaccharides as a marker of tumor progression in human breast and colon neoplasia. Cancer Res. 51, 718–723.

[20] Seelentag, W.K., Li, W.P., Schmitz, S.F., Metzger, U., Aeberhard, P., Heitz, P.U. and Roth, J. (1998) Prognostic value of beta1,6-branched oligosaccharides in human colorectal carcinoma. Cancer Res. 58, 5559–5564.

[21] Murata, K., Miyoshi, E., Kameyama, M., Ishikawa, O., Kabuto, T., Sasaki, Y., Hiratsuka, M., Ohigashi, H., Ishiguro, S., Ito, S., Honda, H., Takemura, F., Taniguchi, N. and Imaoka, S. (2000) Expression of *N*-acetylglucosaminyltransferase V in colorectal cancer correlates with metastasis and poor prognosis. Clin. Cancer Res. 6, 1772–1777.

[22] Dosaka-Akita, H., Miyoshi, E., Suzuki, O., Itoh, T., Katoh, H. and Taniguchi, N. (2004) Expression of *N*-acetylglucosaminyltransferase V is associated with prognosis and histology in non-small cell lung cancers. Clin. Cancer Res. 10, 1773–1779.
[23] Inamori, K., Mita, S., Gu, J., Mizuno-Horikawa, Y., Miyoshi, E., Dennis, J.W. and Taniguchi, N. (in press) Demonstration of the expression and the enzymatic activity of *N*-acetylglucosaminyltransferase IX in the mouse brain. Biochim Biophys Acta.
[24] Bown, N., Cotterill, S., Lastowska, M., O'Neill, S., Pearson, A.D., Plantaz, D., Meddeb, M., Danglot, G., Brinkschmidt, C., Christiansen, H., Laureys, G., Speleman, F., Nicholson, J., Bernheim, A., Betts, D.R., Vandesompele, J. and Van Roy, N. (1999) Gain of chromosome arm 17q and adverse outcome in patients with neuroblastoma. N. Engl. J. Med. 340, 1954–1961.
[25] Lastowska, M., Cotterill, S., Bown, N., Cullinane, C., Variend, S., Lunec, J., Strachan, T., Pearson, A.D. and Jackson, M.S. (2002) Breakpoint position on 17q identifies the most aggressive neuroblastoma tumors. Genes Chromosomes Cancer 34, 428–436.
[26] Yamamoto, H., Swoger, J., Greene, S., Saito, T., Hurh, J., Sweeley, C., Leestma, J., Mkrdichian, E., Cerullo, L., Nishikawa, A., Ihara, Y., Taniguchi, N. and Moskal, J.R. (2000) Beta1,6-*N*-acetylglucosamine-bearing *N*-glycans in human gliomas: implications for a role in regulating invasivity. Cancer Res. 60, 134–142.
[27] Guo, H.B., Lee, I., Bryan, B.T. and Pierce, M. (2005) Deletion of mouse embryo fibroblast *N*-acetylglucosaminyltransferase V stimulates alpha5beta1 integrin expression mediated by the protein kinase C signaling pathway. J. Biol. Chem. 280, 8332–8342.
[28] Dawson, G., Moskal, J.R. and Dawson, S.A. (2004) Transfection of 2,6 and 2,3-sialyltransferase genes and GlcNAc-transferase genes into human glioma cell line U-373 MG affects glycoconjugate expression and enhances cell death. J. Neurochem. 89, 1436–1444.

MOLECULAR AND CELLULAR BIOLOGY, Apr. 2006, p. 2758–2771 Vol. 26, No. 7
0270-7306/06/$08.00+0 doi:10.1128/MCB.26.7.2758–2771.2006

Overlapping Roles for Homeodomain-Interacting Protein Kinases Hipk1 and Hipk2 in the Mediation of Cell Growth in Response to Morphogenetic and Genotoxic Signals†

Kyoichi Isono,[1] Kazumi Nemoto,[1] Yuanyuan Li,[2] Yuki Takada,[1] Rie Suzuki,[1] Motoya Katsuki,[3] Akira Nakagawara,[2] and Haruhiko Koseki[1]*

RIKEN Research Center for Allergy and Immunology, 1-7-22 Suehiro, Tsurumi-ku, Yokohama 230-0045, Japan[1]; Chiba Cancer Center Research Institute, 666-2 Nitona, Chuoh-ku, Chiba 260-8717, Japan[2]; National Institute for Basic Biology, Okazaki National Research Institute, Okazaki, Japan[3]

Received 5 September 2005/Returned for modification 3 October 2005/Accepted 3 January 2006

Homeodomain-interacting protein kinase 1 (*Hipk1*), 2, and 3 genes encode evolutionarily conserved nuclear serine/threonine kinases, which were originally identified as interacting with homeodomain-containing proteins. Hipks have been repeatedly identified as interactors for a vast range of functional proteins, including not only transcriptional regulators and chromatin modifiers but also cytoplasmic signal transducers, transmembrane proteins, and the E2 component of SUMO ligase. Gain-of-function experiments using cultured cells indicate growth regulatory roles for Hipks on receipt of morphogenetic and genotoxic signals. However, *Hipk1* and *Hipk2* singly deficient mice were grossly normal, and this is expected to be due to a functional redundancy between Hipk1 and Hipk2. Therefore, we addressed the physiological roles of Hipk family proteins by using *Hipk1 Hipk2* double mutants. *Hipk1 Hipk2* double homozygotes are progressively lost between 9.5 and 12.5 days postcoitus and frequently fail to close the anterior neuropore and exhibit exencephaly. This is most likely due to defective proliferation in the neural fold and underlying paraxial mesoderm, particularly in the ventral region, which may be attributed to decreased responsiveness to Sonic hedgehog signals. The present study indicated the overlapping roles for Hipk1 and Hipk2 in mediating cell proliferation and apoptosis in response to morphogenetic and genotoxic signals during mouse development.

Homeodomain-interacting protein kinases (HIPKs) compose an evolutionarily conserved protein family in eukaryotes (37). Based on database screening, it appears that three closely related homologous genes encoding Hipks are conserved in vertebrates, including humans, mice, dogs, cows, and frogs (H. Koseki, unpublished). Mammalian HIPK1, HIPK2, and HIPK3 proteins were originally identified as nuclear protein kinases that function as corepressors for various homeodomain-containing transcriptional regulators, at least in part by forming a complex with Groucho and a histone deacetylase complex (7, 37). There is extensive structural similarity exhibited by the HIPKs with respect to their protein kinase domains, homeoprotein interaction domains, PEST sequences, and C-terminal regions enriched by tyrosine and histidine (YH domains). Although HIPK proteins are mainly found in the nucleus with a novel dot-like subnuclear distribution, which partially overlaps promyelocytic leukemia (PML) nuclear bodies, they are nevertheless also found in the cytoplasm (16, 44, 46). HIPKs have been consistently identified as interactors for a vast range of functional proteins, including not only transcriptional regulators and chromatin modifiers but also cytoplasmic signal transducers, transmembrane proteins, and the E2 component of SUMO ligase (11, 14, 19, 25, 30, 31, 36, 38, 39, 40, 45, 51, 55, 57, 60, 63, 64). These observations suggest that HIPKs have a role in the transcriptional regulation, signal transduction, and regulation of protein stability.

Recently, the growth regulatory functions of HIPKs have been intensively investigated. HIPK1 and HIPK2 have been shown to phosphorylate and activate p53, resulting in the enhancement of p53-dependent transcription, cell growth regulation, and apoptosis initiation upon genotoxic insult (12, 13, 14, 30, 39, 46, 57). Independent of the p53 pathway, HIPK2 also appears to promote apoptosis upon genotoxic stress by down-regulating the transcriptional corepressor C-terminal binding protein (CtBP) (68, 69). In the cytoplasm, it has been shown that HIPK3 transduces proapoptotic signals by death receptors through interaction with TRADD and FADD (55). In particular, HIPK1 appears to be a novel signal transducer in tumor necrosis factor alpha-induced apoptosis signaling, activating the apoptosis signal regulating kinase 1/c-Jun N-terminal kinase/p38 mitogen-activated protein kinase signaling cascade (40). A proapoptotic function of HIPK2 has also been proposed in primary neuronal cells (15, 65). Targeted deletion of the *Hipk2* locus leads to a reduction in apoptosis and an increase in the trigeminal ganglion, whereas overexpression of HIPK2 induces apoptosis in cultured sensory neurons. It is, however, intriguing that the results from a study which used *Hipk1*$^{-/-}$ mouse embryonic fibroblasts (MEFs) transformed by *E1A* and *H*-Ras oncogenes suggested antiapoptotic and oncogenic roles for HIPK1 (39). Therefore, taken together, these findings suggest that HIPK proteins are involved in the control of cell growth in response to various extracellular stimuli and that their functions are also affected by intrinsic cellular

* Corresponding author. Mailing address: RIKEN Research Center for Allergy and Immunology, 1-7-22 Suehiro, Tsurumi-ku, Yokohama 230-0045, Japan. Phone: 81-45-503-9689. Fax: 81-45-503-9688. E-mail: koseki@rcai.riken.jp.

† Supplemental material for this article may be found at http://mcb.asm.org/.

issues, such as the cell lineage, developmental stage, genotoxic stress status, and so on.

It has been suggested that HIPK proteins mediate growth regulation in response not only to genotoxic stress and tumor necrosis factor alpha signaling but also to Wnt and transforming growth factor β (TGF-β) signals. HIPK2 is involved in Wnt-1-dependent phosphorylation and subsequent degradation of c-Myb, which may in turn regulate both the proliferation and apoptosis of hematopoietic cells (36). HIPK2 is also capable of forming a multimeric complex with Axin, a common denominator of Wnt signaling, by regulating the cellular level of β-catenin and p53 (57). Similarly, HIPK2 appears to be required for the inhibition of bone morphogenetic protein (BMP)-induced transcriptional activation by forming a complex with c-Ski and Smad1/4 and regulates TGF-β-induced Jun N-terminal kinase activation and apoptosis (26, 31). Taking these results together, it has been hypothesized that HIPKs recognize multiple cellular inputs for the regulation of cell proliferation and apoptosis by regulating the activity of their interacting proteins and subsequently the transcription of the various target genes. Since Wnt and TGF-β family proteins are essential signaling molecules for the development of various organs, it could be expected that HIPK proteins might play a decisive role during embryogenesis by regulating various morphogenetic signal transductions.

The physiological roles of HIPK family proteins have been addressed by generating mutant alleles for *Hipk1* and *Hipk2* genes. Unexpectedly, however, *Hipk1* and *Hipk2* singly deficient mice were grossly normal and fertile (39, 65). Because of structural and functional similarity between HIPK1 and HIPK2, we hypothesized that single-mutant phenotypes for *Hipk1* and *Hipk2* deficiencies may represent some of the functions of HIPK family proteins based on mutually compensative properties. To address this possibility, we have generated *Hipk1 Hipk2* double mutants by crossing newly generated mutant alleles for both genes and have examined doubly deficient phenotypes. $Hipk1^{-/-}$ $Hipk2^{-/-}$ double-mutant embryos are progressively lost between 9.5 and 12.5 days postcoitus (dpc), whereas single mutants survive birth. By using compound mutants, we show that Hipk1 and Hipk2 act in synergy to mediate growth regulation upon genotoxic and morphogenetic signals. Hipks may be involved in the integration of various extracellular stimuli and the mediation of appropriate cellular responses during embryogenesis.

MATERIALS AND METHODS

Histological and skeletal analyses. RNA in situ hybridization, terminal deoxynucleotidyltransferase-mediated dUTP-biotin nick end labeling (TUNEL) with an in situ cell death detection kit (AP; Roche), bromodeoxyuridine (BrdU) incorporation analysis, and skeletal preparations were all performed as described previously (23).

Antibodies to mouse Hipk1 and Hipk2. To generate mouse Hipk1- and Hipk2-specific monoclonal antibodies, glutathione *S*-transferase (GST)–Hipk1 (amino acids 702 to 925) and GST-Hipk2 (amino acids 898 to 1051) fusions were purified and injected into BALB/c mice. Consequently, three and five independent hybridoma clones, H1-1, 3H5, and 3G6 against Hipk1 and 1F11, 2D1, 3F7, 3C5, and 3E9 against Hipk2, respectively, were obtained. The H1-1 clone was used for immunostaining while the 2D1 and 3E9 clones were used for immunostaining, immunoblotting, and immunoprecipitation (IP). In addition to the monoclonal antibodies, a rabbit polyclonal antibody against the GST-Hipk2 fusion (T. K. Craft, Japan) was produced.

Immunostaining. Mouse *Hipk1* and *Hipk2* full-length cDNAs were isolated by reverse transcriptase (RT)-PCR with mouse embryonic RNA. Myc-tagged *Hipk1* and *Hipk2* were subcloned into the expression vector pCXN2 (a gift from H. Niwa) at the EcoRI site. These constructs were used for transfection into U2-OS cells with Lipofectamine 2000 (Invitrogen). After 24 h, cells were fixed in 4% paraformaldehyde for 5 min, permeabilized in 0.4% Triton X for 5 min, and subjected to immunofluorescent staining with anti-Myc (9E10) antibody or the anti-Hipk2 or PML (H-238; Santa Cruz Biotechnology) rabbit polyclonal antibody and then visualized by LSM510 confocal microscope (Carl Zeiss). To address subcellular localization of endogenous Hipk1 and Hipk2, MEFs were double-stained with H1-1 and the Hipk2 polyclonal antibody or 2D1 and the anti-PML antibody. The visualization was carried out with an imaging system consisting of an inverted IX71 microscope with UPlanSApo (magnification, 100×; numerical aperture, 1.40; oil; Olympus), a high-speed spinning disk confocal unit equipped with an ArKr laser system (CSU10; Yokogawa Electric Corp., Japan), and a charge-coupled-device camera (ORCA-AG; Hamamatsu Photonics).

Generation of $Hipk1^{-/-}$ $Hipk2^{-/-}$ mice. Approximately 16.5-kb and 17.5-kb genomic clones for *Hipk1* and *Hipk2*, respectively, were obtained from a λFIX phage library of 129SVJ mice. Each genomic structure was determined by restriction mapping, Southern blotting, and sequencing. The *Hipk1*-targeting vector had the 5′ arm of the XhoI-BamHI fragment (5 kb) from the genomic clone and the 3′ arm of the PCR fragment lacking the initiation codon (1.4 kb) inserted by the *neo* cassette from pHR68 (a gift from T. Kondo) and the *tk* cassette flanked by the 5′ arm. The *Hipk2*-targeting vector had the 5′ arm of the BamHI fragment (3 kb) and the 3′ arm of the BamHI-EcoRI fragment (2.2 kb) from the genomic clone inserted by the *neo* cassette from pMC1-*neo* poly(A) and the *tk* cassette. Germ line chimeras were made with these vectors as described previously (1). Targeted heterozygous mice were backcrossed onto C57BL/6 mice more than three times and intercrossed to obtain homozygous mice. In addition, *Hipk1 Hipk2* double mutants were generated by crossing between *Hipk1* and *Hipk2* single mutants, and $Hipk1^{-/-}$ $Hipk2^{-/-}$ males and females were mainly maintained for embryological analyses. *Hipk1 Hipk2* double mutants were crossed with *p53* mutant mice (24) to generate *p53 Hipk1 Hipk2* triple mutants.

Immunoprecipitation. Whole-cell extracts were prepared by sonicating an 11.5 dpc embryo in 400 μl of IP buffer (20 mM HEPES [pH 7.8], 10% [vol/vol] glycerol, 150 mM KCl, 0.2 mM EDTA, 1 mM dithiothreitol) containing 4 mM Pefabloc SC (Roche). Lysates were precleared with 50 μl of 50% (vol/vol) protein G-Sepharose at 4°C for 60 min and then incubated for 90 min with *Hipk2* antibody (2D1)-bound protein G, which had already been prepared by mixing 100 μl of the 2D1 culture supernatant with 20 μl of 50% (vol/vol) protein G-Sepharose and 300 μl IP buffer for 90 min. After this 90-min incubation period, protein-bound protein G was washed five times with 800 μl IP buffer, boiled in sodium dodecyl sulfate-sample buffer, separated on 6.5% denaturing polyacrylamide gels, and then analyzed by Western blotting using the Hipk2 antibody (2D1).

Cell culture. MEFs were prepared from 12.5 dpc mouse embryos (33), which were genotyped with yolk sac DNAs and then stored at −80°C. The MEFs were grown in Dulbecco's minimal essential medium supplemented with 10% fetal calf serum and 1% (wt/vol) penicillin/streptomycin on 6-cm dishes at 37°C under 7% CO_2. At passage 4, the culture medium was removed and cells were irradiated with UV (15 or 50 J/m^2) with UV cross-linker (UV Products, Cambridge, United Kingdom) and then recultured in the same medium. Subsequently, at the indicated periods, cells were collected and the trypan blue-stained dead cells and unstained living cells were counted. In addition, these cells were sonicated, and each lysate (30 μg) was subjected to Western blot analysis with anti-p53 (M-19), anti-Bax (B-9), and anti-p21 (F-5) from Santa Cruz Biotechnology, anti-cleaved caspase 3 from Cell Signaling Technology, and anti-CtBP-1 from Upstate. Alternatively, cells on coverslips 12 h after UV (15 and 50 J/m^2) exposure were subjected to a TUNEL assay with the kit described above and then counterstained with eosin.

Luciferase reporter assay. Human lung carcinoma H1299 cells ($p53^{-/-}$) were grown in RPMI 1640 medium supplemented with 10% fetal calf serum and antibiotics and transfected with the Lipofectamine Plus transfection kit (Invitrogen, Grand Island, NY) according to the manufacturer's protocol. Briefly, H1299 cells were seeded at a density of 5×10^4 cells/well in a 12-well tissue culture dish and then cotransfected with 100 ng of p53-responsive luciferase reporter constructs carrying *Bax* and $p21^{WAF1}$ promoter, 10 ng of pRL-TK (Promega), and 25 ng of the human or mouse p53 expression plasmid in either the presence or absence of increasing amounts of the pCXN2-Myc-Hipk1 or -Hipk2 construct as described previously (64). The total amounts of DNA used in each transfection were kept constant (510 ng/transfection) using pcDNA3. Luciferase assays were performed 48 h posttransfection with a dual luciferase reporter assay system

(Promega) according to the manufacturer's instructions. To examine the degree of transactivation by DNA damage, transfected cells were exposed to UV (15 and 50 J/m^2) at 24 h posttransfection or treated with cisplatin (Sigma Chemical Co., St. Louis, MO) at a final concentration of 20 μM for 24 h.

Explant culture of presomitic mesoderm and RT-PCR. Strips of the anterior half of the unsegmented paraxial mesoderm were isolated from 9.5 dpc mouse embryos by a combination of dispase treatment and subsequent surgical dissection using a tungsten needle, essentially following a previously described method (21). Mouse tissues were embedded in collagen gels and cultured as described previously (21). Bacterially expressed recombinant Shh protein was added to the culture to a concentration of 100 ng/ml. After 2 days of culture, total RNA was extracted from the explants in collagen gels as described previously (21). Each sample was reverse transcribed by reaction with oligo(dT) primers in a volume of 20 μl. The product of this reaction was serially diluted in a ratio of 3:1, and eventually amounts equivalent to 3, 1, 0.33, 0.11, 0.037, 0.012, 0.0041, and 0.00147 μl of the original reaction volume were subjected to PCR for *Pax1*, *Twist*, and *Hprt* (21). The amounts of total cDNA were corrected by comparing the *Hprt* signal intensities.

RESULTS

The expression of *Hipk* genes during embryogenesis. A prerequisite of the hypothesis that Hipk1 and Hipk2 act in a redundant and mutually compensable manner is the coexpression and colocalization of Hipk family proteins. We therefore compared the expressions of *Hipk* genes during embryogenesis, particularly around 9.5 dpc, at which embryonic stage various inductions that are required for subsequent organ development take place. The expression of *Hipk1* is seen ubiquitously through 8.5 to 10.5 dpc but is slightly enhanced in the neural tube at 10.5 dpc (16; K. Isono, unpublished). *Hipk2* was intensely expressed in the neural tissues, including optic and otic vesicles and newly generated paraxial mesoderm, while other tissues also expressed lower but nevertheless significant amounts of *Hipk2* at 9.5 dpc (Fig. 1A, B, and G) (52). The section at the level of the midbrain revealed the expression in this region and in the emerging and migrating neural crest cells and branchial arches and membranes (Fig. 1C, D, and E). Interestingly, the expression was more intense in the neural crest-derived cells localizing in the vicinity of the surface ectoderm. In the otic vesicle, intense expression was also seen at the region juxtaposed to the surface ectoderm (Fig. 1F). In the prospective trunk region, *Hipk2* expression in the neural tube was slightly more intense in the dorsal than the ventral region and was not seen in the floor plate or the notochord (Fig. 1H). *Hipk2* expression in the paraxial mesoderm was transiently increased in the cranial part of the presomitic mesoderm and newly segmented somites (Fig. 1J). After de-epithelization of the somites, the expression was lower in the sclerotome than in the dermomyotome and was not seen in the myotome (Fig. 1I and J). Therefore, *Hipk2* is expressed in most tissues except for the notochord, floor plate, and myotome. In contrast, *Hipk3* was exclusively expressed in the myocardial wall of the heart primordium and myotome (Fig. 1K, L, and M). These observations indicate that there is coexpression of *Hipk1* and *Hipk2* in various embryonic tissues.

Coexpression and colocalization of Hipk1 and Hipk2 gene products. We went on to examine whether endogenous Hipk1 and Hipk2 proteins were coexpressed in embryonic cells by immunofluorescence. Primary MEFs derived from 12.5 dpc fetuses were used. In all MEFs examined, both proteins were expressed and exhibited punctate localization throughout the nucleus apart from the nucleoles (Fig. 1N, left). Higher magnification views revealed that Hipk1 and Hipk2 were condensed to numerous speckles, which were surrounded by less-condensed foggy domains (Fig. 1N, middle). Condensed speckles for Hipk1 and Hipk2 were mostly separated, and overlapping regions were consequently limited. We also observed their punctate distributions in cytoplasm. Minor fractions of Hipk1 and Hipk2 were contained in PML nuclear bodies as observed in various cell lines (Fig. 1N, right) (K. Isono, unpublished). Therefore, Hipk1 and Hipk2 were coexpressed in primary MEFs. Inclusion to similar extents of both Hipk1 and Hipk2 in PML nuclear bodies may partly indicate their functional similarity.

We next examined the colocalization of Hipk1 and Hipk2 following overexpression, since transiently expressed Hipk1 and Hipk2 in cultured cells were known to localize to subnuclear speckles, which were much larger in size than those seen in MEFs (14, 16, 30, 37, 44). We examined the subnuclear localization of Hipk1 and Hipk2 in U2-OS cells that had been transfected by expression vectors for Myc-tagged Hipk1 and wild-type Hipk2, and these proteins were detected by immunofluorescence with anti-Myc and -Hipk2 antibodies. Under this condition, Hipk1 and Hipk2 strongly colocalized to subnuclear speckles (Fig. 1O). Hipk1 also exhibited a partial colocalization with PML nuclear bodies as well as Hipk2 (Fig. 1P) (14, 16, 30). This may imply that Hipk1 and Hipk2 are potentially capable to colocalize to subnuclear domains in certain cellular contexts, which again indicates their functional similarity.

Generation of *Hipk1 Hipk2* doubly deficient mice. To generate *Hipk1 Hipk2* doubly deficient mice, we independently generated *Hipk1* and *Hipk2* mutant alleles. Since the kinase domains have been shown to be essential for mediating transcriptional repression, the intention was to generate mutant alleles lacking their kinase domains (Fig. 2A and B) (7, 37). The N-terminal halves of the kinase domains of Hipk1 and Hipk2 were encoded by exons containing the start codon. For *Hipk1* mutagenesis, a targeting vector was designed to replace a genomic fragment containing the start codon with a neomycin-resistant (Neo^r) gene cassette (Fig. 2A). For *Hipk2* knockout, a targeting vector was generated to replace the BamHI fragment encoding the C-terminal part of the exon containing the start codon and the flanking intronic region with the Neo^r cassette (Fig. 2B). Both mutations were transmitted into the germ line, and heterozygotes were crossed to generate the homozygotes. Both single homozygous mutant mice were grossly normal and born in a Mendelian ratio as reported for other alleles (39, 65). RT-PCR revealed that both mutations impaired the expression of *Hipk1* and *Hipk2* at least at the regions encoding the kinase domains (Fig. 2C and D). Immunoprecipitation-Western analysis using a monoclonal antibody against the interacting domain of Hipk2 further supported depletion of intact Hipk2 protein in the homozygotic mutants (Fig. 2D). However, we cannot exclude the presence of the C-terminally truncated proteins in both mutants.

Embryonic lethality and exencephaly in *Hipk1 Hipk2* double homozygotes. To explore the phenotypes of *Hipk1*$^{-/-}$ *Hipk2*$^{-/-}$ mice, double heterozygous mice which were viable and fertile were crossed, and naturally delivered newborn pups were genotyped. We found that all of the double homozygotes and about half of the *Hipk1*$^{+/-}$ *Hipk2*$^{-/-}$ embryos were lost during

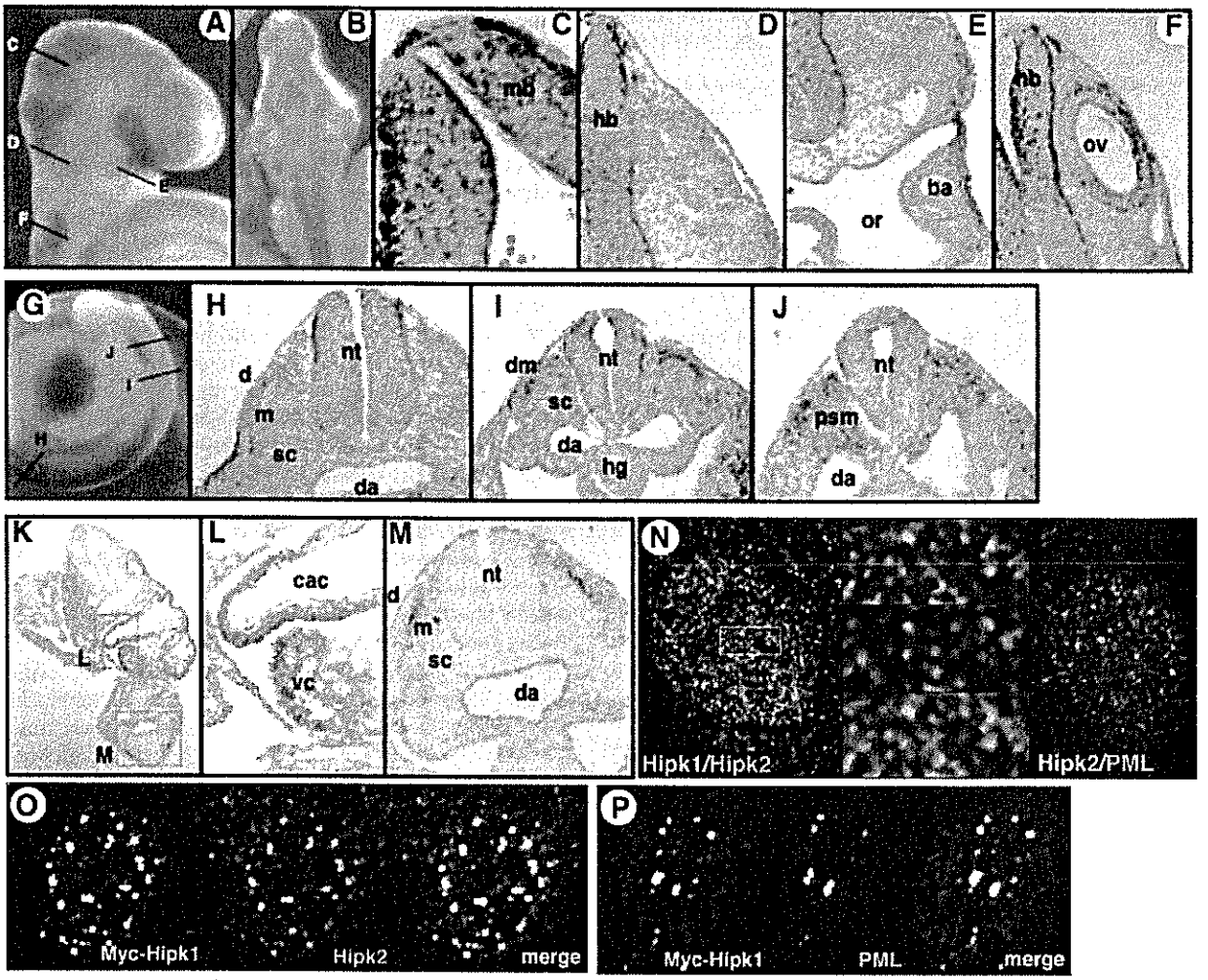

FIG. 1. Expression of *Hipk2* and *Hipk3* in 9.5 dpc embryos, and subnuclear localization of Hipk1 and Hipk2. (A) Lateral view of *Hipk2* expression in the cranial region. Note the intense expression in the neural tissue, including optic vesicle, mid- and hindbrains, and otic vesicle, compared with the weaker expression in the mesodermal tissue. The sections that are shown in panels C, D, E and F are indicated. (B) Dorsal view of *Hipk2* expression in the cranial region. (C) *Hipk2* expression at the level of midbrain (mb). Note the intense expression in the migrating neural crest cells. (D) *Hipk2* expression at the level of hindbrain (hb). (E) *Hipk2* expression around the oropharynx (or) and first branchial arch (ba). (F) *Hipk2* expression at the level of the otic vesicle (ov). (G) Lateral view of *Hipk2* expression in the caudal region. Note the intense expression in the presomitic mesoderm and first somite. The sections shown in panels H, I, and J are indicated. (H) *Hipk2* expression at the level of the prospective interlimb region. Abbreviations: d, dermatome; da, dorsal aorta; m, myotome; nt, neural tube; sc, sclerotome. (I) *Hipk2* expression at the level of de-epithelizing somite. Abbreviations: dm, dermomyotome; hg, hindgut. (J) *Hipk2* expression at the level of presomitic mesoderm (psm). (K) Lower-magnification view of *Hipk3* expression. The regions shown in panels L and M are indicated by boxes. (L) Higher-magnification view of *Hipk3* expression. Abbreviations: cac, common atrial chamber of the heart; vc, ventricular chamber of the heart. (M) Higher-magnification view of *Hipk3* expression. (N) Coexpression of Hipk1 and Hipk2 in primary MEFs. (Left) Coexpression of endogenous Hipk1 (green) and Hipk2 (red) in a MEF. (Middle) Higher-magnification views of the framed region in the left panel: endogenous Hipk1 (top), endogenous Hipk2 (middle), and merged image (bottom). (Right) A minor fraction of endogenous Hipk2 (green) is localized in PML bodies (red). (O) Subcellular localization of transfected Myc-tagged Hipk1 (left, green) and Hipk2 (middle, red) in U2OS cells. A merged image is shown in the right panel (yellow). (P) Subcellular localization of transfected Myc-tagged Hipk1 (left, green) and endogenous PML (middle, red) in U2OS cells. A merged image is shown in the right panel (yellow).

gestation against their expected values predicted by Mendelian fashion (Table 1). We next examined at which stage of gestation *Hipk1*$^{-/-}$ *Hipk2*$^{-/-}$ embryos were affected. *Hipk1*$^{-/-}$ *Hipk2*$^{+/-}$ mice which were grossly normal and fertile were mated, and the embryos were visually inspected under the stereomicroscope at 8.5, 9.5, 10.5, and 12.5 dpc (Table 2). *Hipk1*$^{-/-}$ *Hipk2*$^{-/-}$ embryos were indistinguishable from the single homozygotes at 8.5 dpc. At 9.5 dpc, however, 7 out of 24 were dead and being absorbed, and 14 out of 17 live embryos were smaller and developmentally delayed compared to *Hipk1*$^{-/-}$ *Hipk2*$^{+/+}$ or *Hipk1*$^{-/-}$ *Hipk2*$^{+/-}$ embryos. Most of the double homozygous mutants were dead before 12.5 dpc.

About half of the surviving *Hipk1*$^{-/-}$ *Hipk2*$^{-/-}$ and a small subset of the *Hipk1*$^{-/-}$ *Hipk2*$^{+/-}$ embryos failed to close the anterior neuropore and exhibited exencephaly at 9.5 and 11.5 dpc (Fig. 3A, B, and C; Table 3). This defect was characterized

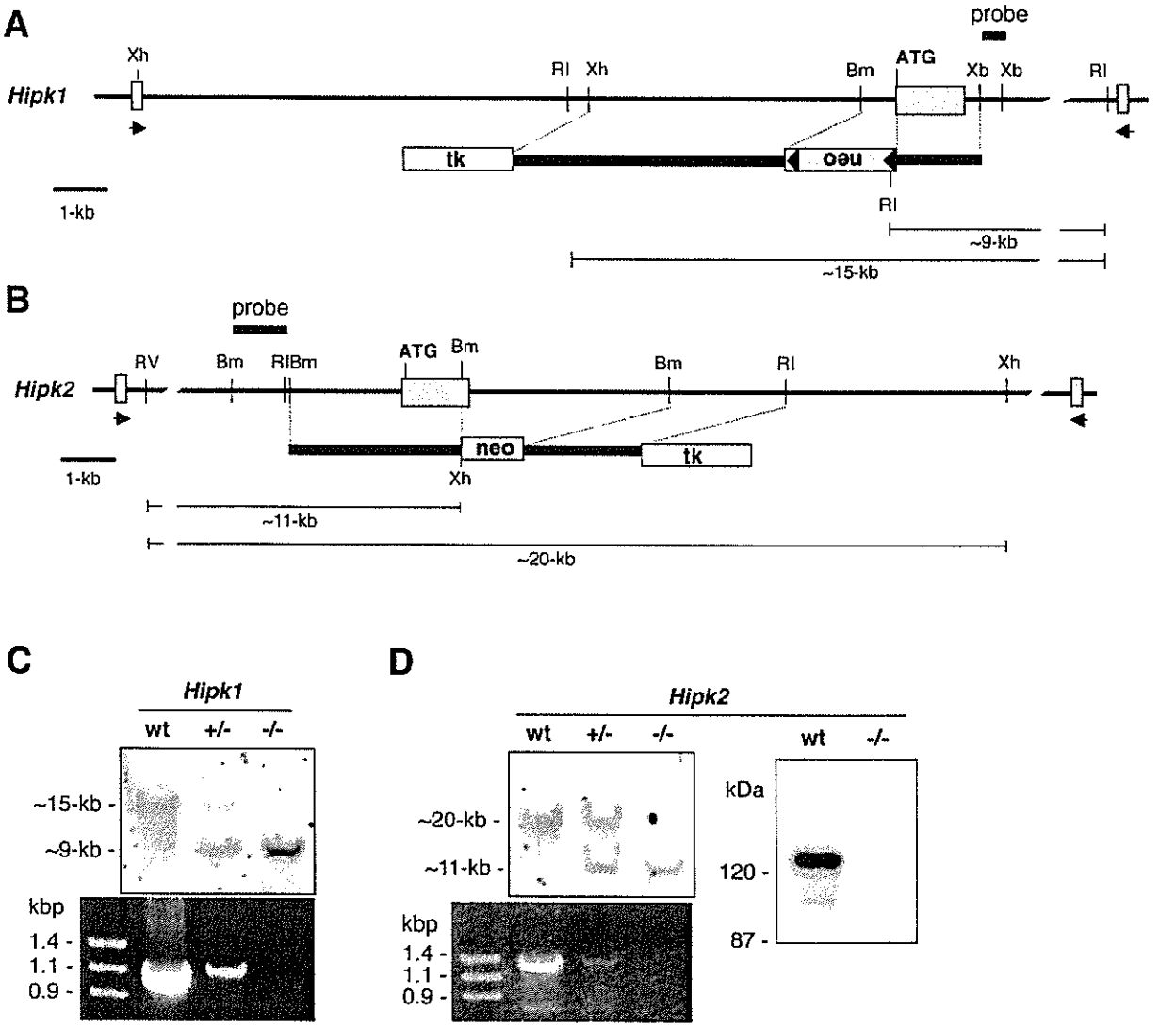

FIG. 2. Generation of *Hipk1* and *Hipk2* mutant alleles. (A and B) Genomic organization of the *Hipk1* and *Hipk2* loci around the exon containing the start codon (ATG) and their targeting constructs. Exonic regions are shown by shaded boxes. The position of each external probe (probe) is indicated. Arrowheads indicate primers used for RT-PCR. Abbreviations: neo, neomycin-resistant gene cassette; tk, herpes simplex virus thymidine kinase gene; Bm, BamHI; RI, EcoRI; RV, EcoRV; Xb, XbaI; Xh, XhoI. (C) Top: Southern blot analysis of *Hipk1* mutant allele. Genomic DNAs from respective genotypes are digested with EcoRI and probed. Bottom: RT-PCR analysis of *Hipk1* mRNA with total RNAs from 12.5 dpc embryos. wt, wild type. (D) Top left: Southern blot analysis of *Hipk2* mutant allele. Genomic DNAs from respective genotypes are digested with EcoRV and XhoI and probed. Bottom left: RT-PCR analysis of *Hipk2* mRNA with total RNAs from 12.5 dpc embryos. Right: IP-Western blot analysis of Hipk2 gene products in the wild-type (wt) and homozygous mutant (−/−) embryos at 11.5 dpc. Precipitates of anti-Hipk2 antibody were blotted with the Hipk2 antibody.

by an overgrowth of neural tissue, usually confined to the region of the fore- and midbrain but occasionally affecting the hindbrain (Fig. 3B and C). Apart from this particular neurological defect, we observed failure in lens vesicle formation associated with disorientation of optic cups and fusion of dorsal root ganglia (DRG) (Fig. 3D and E). Since embryonic survival was influenced by the dosage of *Hipk* mutations, we addressed whether *Hipk* dosage affects the incidence of neural tube closure defect (NTD) as well. Therefore, we crossed *Hipk* compound mutants and examined *Hipk* genotypes at 10.5 and 11.5 dpc, because the anterior neuropore closes during the 15- to 20-somite stage. In addition, we examined the gender effect,

TABLE 1. Survival of *Hipk* compound mutant mice[a]

Genotype	No. of mice	
	Born	Expected
$Hipk1^{+/+}$ $Hipk2^{+/+}$	11	9.5
$Hipk1^{+/-}$ $Hipk2^{+/+}$	29	19
$Hipk1^{+/+}$ $Hipk2^{+/-}$	21	19
$Hipk1^{-/-}$ $Hipk2^{+/+}$	13	9.5
$Hipk1^{+/+}$ $Hipk2^{-/-}$	9	9.5
$Hipk1^{+/-}$ $Hipk2^{+/-}$	42	38
$Hipk1^{-/-}$ $Hipk2^{+/-}$	19	19
$Hipk1^{+/-}$ $Hipk2^{-/-}$	8	19
$Hipk1^{-/-}$ $Hipk2^{-/-}$	0	9.5

[a] Mating type: $Hipk1^{+/-}$ $Hipk2^{+/-}$ × $Hipk1^{+/-}$ $Hipk2^{+/-}$.

TABLE 2. Survival of *Hipk1*$^{-/-}$ *Hipk2*$^{-/-}$ embryos during gestation[a]

Genotype	No. of live embryos (no. of embryos being resorbed) at indicated dpc:			
	8.5	9.5	10.5	12.5
Hipk1$^{-/-}$ *Hipk2*$^{+/+}$	7 (0)	34 (2)	22 (2)	14 (0)
Hipk1$^{-/-}$ *Hipk2*$^{+/-}$	12 (0)	43 (3)	30 (4)	23 (0)
Hipk1$^{-/-}$ *Hipk2*$^{-/-}$	5 (0)	24 (7)	12 (7)	1 (5)

[a] Mating type: *Hipk1*$^{-/-}$ *Hipk2*$^{+/-}$ × *Hipk1*$^{-/-}$ *Hipk2*$^{+/-}$.

as the incidence of NTD tends to be higher in females than in males (3, 35, 59). The incidence of NTD in the various *Hipk* mutants had not fully penetrated, even in the *Hipk1*$^{-/-}$ *Hipk2*$^{-/-}$ embryos, although the differences were significant and its penetrance was clearly affected by *Hipk* gene dosage (Table 3). For all genotypes, NTD occurred more frequently in females than in males. We also found that Hipk2 plays a more dominant role than Hipk1 in the suppression of NTD as well as in embryonic survival. Therefore, *Hipk1* and *Hipk2* mutations synergistically affect embryonic survival and neural tube closure.

Embryonic lethality in *Hipk1 Hipk2* double homozygotes involves p53. Female-skewed incidence of NTD has also been reported in *p53*-deficient mice, in which about 30% and 1% of homozygous females and males, respectively, exhibit exencephaly (59). Moreover, there is considerable evidence for functional interactions between HIPKs and p53 in human cells

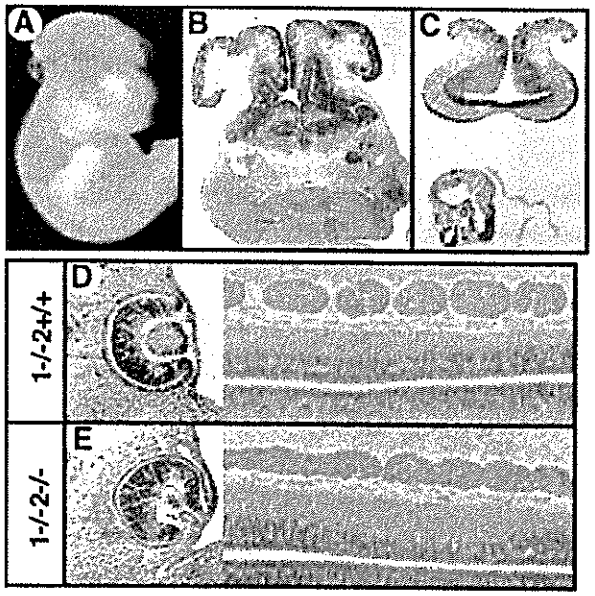

FIG. 3. Exencephaly and other histological abnormalities in *Hipk1*$^{-/-}$ *Hipk2*$^{-/-}$ embryos. (A) Lateral view of 11.5 dpc *Hipk1*$^{-/-}$ *Hipk2*$^{-/-}$ embryos exhibiting exencephaly. (B) Frontal section of 12.5 dpc *Hipk1*$^{-/-}$ *Hipk2*$^{-/-}$ embryos. (C) Frontal section of 9.5 dpc *Hipk1*$^{-/-}$ *Hipk2*$^{-/-}$ embryos. Overgrowth of neural tissue is usually confined to the region of the fore- and midbrain. (D) Normal formation of lens vesicle (left) and DRG (right) in *Hipk1*$^{-/-}$ *Hipk2*$^{+/+}$ embryos. (E) Failure of lens vesicle formation associated with disorientation of optic cups and fusion of DRGs in *Hipk1*$^{-/-}$ *Hipk2*$^{-/-}$ embryos.

TABLE 3. Incidence of NTD in male and female *Hipk* compound mutants

Genotype	Gender	NTD/total[a] (%)
Hipk1$^{-/-}$ *Hipk2*$^{+/+}$	Male	0/37 (0)
	Female	1/36 (2.8)
Hipk1$^{+/+}$ *Hipk2*$^{-/-}$	Male	0/23 (0)
	Female	1/21 (4.8)
Hipk1$^{+/-}$ *Hipk2*$^{+/-}$	Male	0/29 (0)
	Female	1/31 (3.2)
Hipk1$^{-/-}$ *Hipk2*$^{+/-}$	Male	1/62 (1.6)
	Female	5/63 (7.9)
Hipk1$^{+/-}$ *Hipk2*$^{-/-}$	Male	3/39 (7.7)
	Female	4/24 (16.7)
Hipk1$^{-/-}$ *Hipk2*$^{-/-}$	Male	11/28 (39.3)
	Female	10/18 (55.6)

[a] Number of embryos with NTD/total number of embryos with indicated genotype.

(12, 13, 14, 30, 39, 46, 57). These findings prompted us to address whether Hipks act via p53 during mouse development. Triple compound mutants were crossed to *Hipk1 Hipk2* compound mutants, and the morphology and genotype of the embryos were examined at 12.5 dpc. Four exencephalic embryos turned out to be *p53*$^{+/-}$ *Hipk1*$^{-/-}$ *Hipk2*$^{-/-}$, whereas none were *p53*$^{+/+}$ *Hipk1*$^{-/-}$ *Hipk2*$^{-/-}$; this result was surprising given the mating conditions, under which 4.5 embryos in the respective genotypes would have been expected. Although the number of samples examined was not sufficient to draw any statistical conclusions, it is possible that p53 is at least in part involved in the mediation of early embryonic lethality in *Hipk1*$^{-/-}$ *Hipk2*$^{-/-}$ embryos.

To address the molecular basis for this genetic interaction, we examined whether murine Hipk1 and Hipk2 were capable of acting together with murine p53 in the regulation of p53-dependent transcription. H1299 cells (p53$^{-/-}$) were cotransfected with expression vectors encoding human or murine p53 and murine Hipk1 or Hipk2 together with a reporter vector carrying the *p21*^{WAF1} or *Bax* promoter (Fig. 4). Both Hipk1 and Hipk2 increased p53-mediated transactivation of *p21*^{WAF1} and *Bax* promoters via murine p53 to an extent similar to that of the human counterpart. In contrast, Hipk1 or Hipk2 alone had no effect on either promoter. Therefore, Hipk1 and Hipk2 were shown to regulate p53 functions via physical interactions to mediate embryonic survival despite murine p53 lacking serine 46, which is conserved in human p53, phosphorylated by HIPK2, and involved in mediation of apoptosis upon genotoxic stimuli (14, 30, 47). Importantly, cotransfection of Hipk1 and Hipk2 did not exhibit any synergistic effects on the transactivation of p53 (Y. Li and A. Nakagawara, unpublished observations). Synergistic enhancement of respective single-mutant phenotypes in compound mutants might be due to functional redundancy or gene dosage effects rather than cooperation between Hipk1 and Hipk2.

Hipks mediate proliferation during neural and mesodermal development. In most mouse NTD models, NTDs reflect failure of neural fold elevation. Some NTD mutants, including *p53*, *Gadd45a*, and *Terc*, suggest that genes with a basic mitotic function also have a function specific to neural fold elevation (29, 34, 59). Indeed, HIPK family proteins have been shown to play significant roles in the regulation of cell growth and apop-

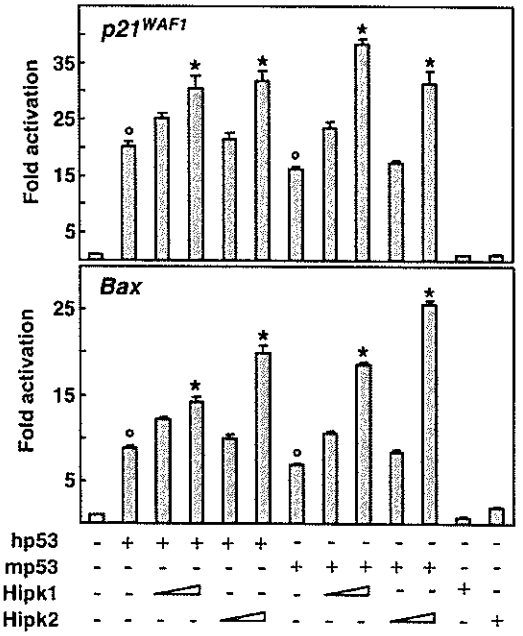

FIG. 4. Hipk1 and Hipk2 enhance p53-dependent transactivation of $p21^{WAF1}$ and *Bax* promoters via murine p53. p53-deficient H1299 cells were transiently cotransfected with the expression plasmid for human p53 (hp53) or murine p53 (mp53) along with luciferase reporter constructs containing $p21^{WAF1}$ (top) or *Bax* (bottom) promoter in the absence or presence of increasing amounts of transfected Hipk1 or Hipk2. Transfection efficiency was standardized against *Renilla* luciferase. The average relative luciferase activities in triplicate experiments are represented by bars. Means ± standard deviations of results are shown as fold induction of luciferase activity compared with number of cells transfected with vacant pcDNA3. Data shown are representative of three independent experiments with similar results. The significance of the differences were evaluated by the Student's *t* test. The bars marked with asterisks indicate significant difference ($P < 0.05$) from the bars indicated by open circles.

tosis in cultured cells and in primary sensory neurons (14, 15, 30, 39, 65). Therefore, we hypothesized that NTD in $Hipk1^{-/-}$ $Hipk2^{-/-}$ embryos may involve changes in cell growth in developing neural tube and paraxial mesoderm because the neural tube closure involves not only the neuroectoderm but also the underlying paraxial mesoderm. We first examined cellular proliferation by labeling 9.5 dpc embryos by BrdU around the level of midbrain/hindbrain boundary and prospective cervicothoracic boundary. We crossed $Hipk1^{-/-}$ $Hipk2^{+/-}$ mice and compared $Hipk1^{-/-}$ $Hipk2^{+/+}$ and $Hipk1^{-/-}$ $Hipk2^{-/-}$ embryos because *Hipk1* single mutants were morphologically normal. In the cranial region, the frequency of mitotic cells in the $Hipk1^{-/-}$ $Hipk2^{-/-}$ neural tube was significantly reduced to 45% and 29% of that of the $Hipk1^{-/-}$ embryos in the dorsal and ventral regions, respectively (Fig. 5A, B, E, F, and I). Proliferation of the cephalic mesoderm of the $Hipk1^{-/-}$ $Hipk2^{-/-}$ embryos was also reduced to 43% of the $Hipk1^{-/-}$ embryos. In the trunk region, proliferation was affected in the ventral but not the dorsal region of the neural tube and in the sclerotomal compartment of the paraxial mesoderm in the $Hipk1^{-/-}$ $Hipk2^{-/-}$ embryos (Fig. 5C, D, G, H, and J). We next investigated the frequency of apoptotic cells in the $Hipk1^{-/-}$ $Hipk2^{+/+}$ and $Hipk1^{-/-}$ $Hipk2^{-/-}$ embryos by TUNEL staining. Although we did not see a significant difference within the neural tube in the cranial region, numbers of apoptotic cells were significantly increased in the condensing trigeminal and facioacoustic neural crest cells (Fig. 5K). In the trunk region, we reproducibly observed more apoptotic outbursts in the sclerotomal compartment in $Hipk1^{-/-}$ $Hipk2^{-/-}$ than $Hipk1^{-/-}$ $Hipk2^{+/+}$ embryos but did not see significant changes in the neural tube. Therefore, Hipks are shown to promote mitosis and repress apoptotic outbursts in a tissue-specific manner during embryogenesis, which could partly be the cause of the defects in neural fold elevation. Interestingly, the fusion of DRGs is caused by an insufficient proliferation of sclerotomal cells, which may fail to provide the mesenchymal cells that separate DRGs, or by defects in craniocaudal specification of the somitic mesoderm (50, 58, 62). Craniocaudal specification and subsequent segmentation of the somites occurs normally, as revealed by the expression of *Uncx4.1* and *Hes5* in $Hipk1^{-/-}$ $Hipk2^{-/-}$ embryos (K. Isono, unpublished). Therefore, DRG fusion may also be at least in part due to impaired proliferation of sclerotomal cells.

Defective *Pax1* induction by Shh in *Hipk* double mutants. We next examined the expression of genes involved in the incidence of NTD in $Hipk1^{-/-}$ $Hipk2^{-/-}$ embryos. It is particularly interesting to investigate the expression of *Twist*, *Shh*, and Shh-dependent genes like *Pax1* and *Pax3* (5, 6, 22). Cranial NTD in *Twist* homozygotes was associated with the reduction of proliferation and expansion of the cranial mesenchyme. Shh is a predominant signaling molecule involved in neural fold elevation, which mediates the proliferation and differentiation of the neural tube and paraxial mesoderm by inducing a series of transcriptional regulators in the ventral regions of the respective tissues (22, 56). We further examined the expression of *Pax1*, which is expressed in the sclerotome in a Shh-dependent manner and is involved in the mediation of the proliferation of sclerotomal cells (22, 62). NTD in the *Pax3* mutant was shown to involve p53, and *Pax3* expression is repressed in the ventral region of the neural tube and paraxial mesoderm by Shh (20, 49).

In the wild-type and $Hipk1^{-/-}$ embryos at 9.5 dpc, *Twist* is expressed in the branchial arches and paraxial and lateral plate mesoderm (Fig. 6A, left). In $Hipk1^{-/-}$ $Hipk2^{-/-}$ embryos, the expression was significantly reduced in the paraxial and lateral plate mesoderms but not in the branchial arches (Fig. 6A, right). *Shh* expression was not significantly changed in the notochord of $Hipk1^{-/-}$ $Hipk2^{-/-}$ embryos but was reduced in the floor plate (Fig. 6B, bottom). Sclerotomal expression of the *Pax1* gene was decreased in $Hipk1^{-/-}$ $Hipk2^{-/-}$ embryos while the expression in the pharyngeal pouches was not significantly changed (Fig. 6B, top). The expression of *Pax3* in the dorsal regions of fore-, mid-, and hindbrain was not grossly changed in $Hipk1^{-/-}$ $Hipk2^{-/-}$ embryos irrespective of exencephaly (K. Isono, unpublished). However, we observed that in the neural tube in $Hipk1^{-/-}$ $Hipk2^{-/-}$ embryos, the *Pax3* expression domain was ventrally expanded (Fig. 6C). Since the expression of *Pax1* and *Pax3* in the paraxial mesoderm and/or neural tube are regulated by Shh, it is likely that Shh signaling is affected in $Hipk1^{-/-}$ $Hipk2^{-/-}$ embryos. To exclude the possibility that the expression of Shh gene products is reduced in double homozygotes, we monitored the expression of *Foxa2* in the floor plate, which is also Shh dependent (56) (Fig. 6D). *Foxa2*

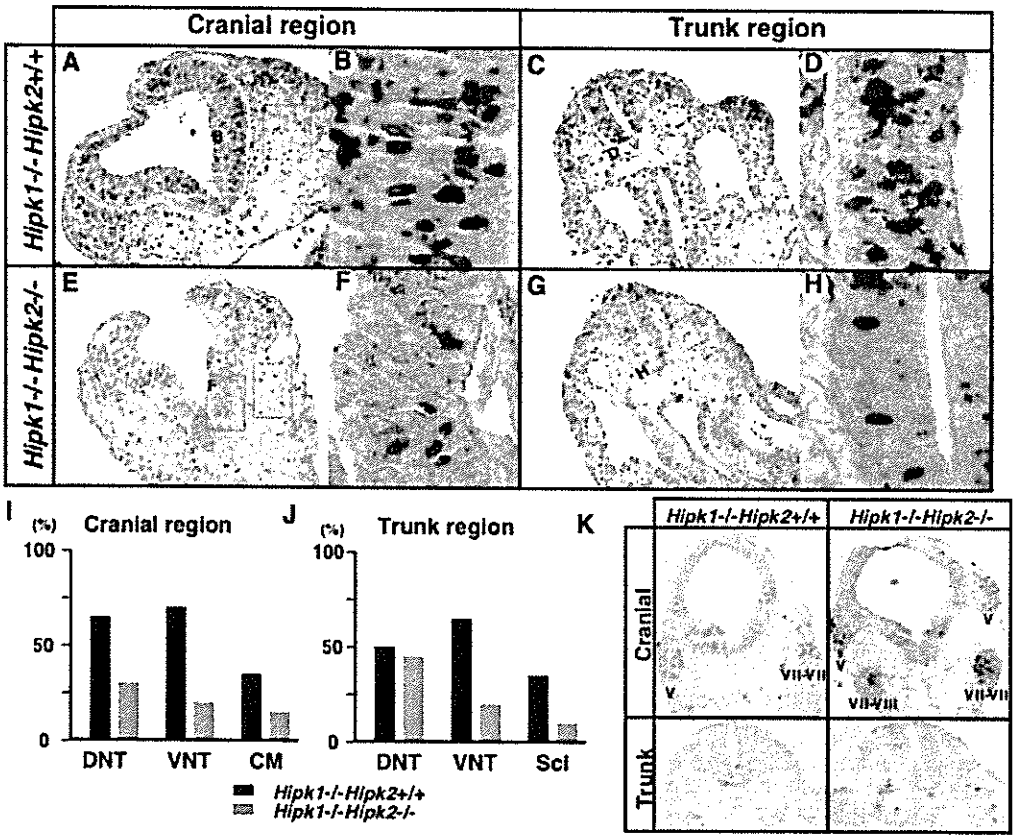

FIG. 5. Reduced mitotic cells and increased apoptotic cells in *Hipk1*$^{-/-}$ *Hipk2*$^{-/-}$ embryos. (A) Distribution of BrdU-positive cells in the cranial region of *Hipk1*$^{-/-}$ *Hipk2*$^{+/+}$ embryos at 9.5 dpc. Frequencies of BrdU-labeled cells were counted in the boxes in the dorsal region of the neural tube (DNT in panels I and J), ventral region of the neural tube (VNT in panels I and J, with a higher magnification shown in panel B) and cephalic mesoderm (CM in panels I and J). (B) Higher magnification of the area indicated by box B in panel A. (C) Distribution of BrdU-positive cells in the prospective trunk regions of *Hipk1*$^{-/-}$ *Hipk2*$^{+/+}$ embryos at 9.5 dpc. Frequencies of BrdU-labeled cells were counted in the boxes in the dorsal region of the neural tube (DNT in panels I and J), ventral region of the neural tube (VNT in panels I and J, with a higher magnification shown in panel D) and sclerotome (Scl in panels I and J). (D) Higher magnification of the area indicated by box D in panel C. (E) Distribution of BrdU-positive cells in the cranial regions of *Hipk1*$^{-/-}$ *Hipk2*$^{-/-}$ embryos at 9.5 dpc. The frequency of BrdU-labeled cells was counted in the areas demarcated by the boxes. (F) Higher magnification of the area indicated by box F in panel E. (G) Distribution of BrdU-positive cells in the prospective interlimb regions of *Hipk1*$^{-/-}$ *Hipk2*$^{-/-}$ embryos at 9.5 dpc. (H) Higher magnification of the area indicated by box H in panel G. (I) Frequency of BrdU-labeled cells in the regions indicated by boxes in the cranial region. DNT, dorsal region of the neural tube; VNT, ventral region of the neural tube; CM, cephalic mesoderm. Means are shown by black (*Hipk1*$^{-/-}$ *Hipk2*$^{+/+}$) and gray (*Hipk1*$^{-/-}$ *Hipk2*$^{-/-}$) bars. (J) Frequency of BrdU-labeled cells in the regions indicated by boxes in the prospective trunk region. Scl, sclerotome. (K) Distribution of apoptotic cells revealed by TUNEL staining in the cranial (top) and prospective trunk (bottom) regions. In the cranial region, sections through the trigeminal (V) and facioacoustic (VII-VIII) neural crest tissues are shown although the section of *Hipk1*$^{-/-}$ *Hipk2*$^{+/+}$ embryo (top left) is oblique. Note the significant apoptotic outbursts in the trigeminal and facioacoustic neural crest tissues of the *Hipk1*$^{-/-}$ *Hipk2*$^{-/-}$ embryo (top right). In the prospective trunk region, apoptotic outbursts are more pronounced in the sclerotomal compartments in the *Hipk1*$^{-/-}$ *Hipk2*$^{-/-}$ embryo (bottom right) than the *Hipk1*$^{-/-}$ *Hipk2*$^{+/+}$ embryo (bottom left).

expression was not changed in the floor plate or the midgut endoderm. Therefore, it is likely that the notochordal expression of Shh protein is unaffected in *Hipk1*$^{-/-}$ *Hipk2*$^{-/-}$ embryos. To examine whether cellular responses might be primarily impaired upon Shh signaling, we cultured explants of unsegmented paraxial mesoderm, as described previously, in the presence of Shh and investigated the *Pax1* expression in *Hipk1*$^{-/-}$ *Hipk2*$^{-/-}$ embryos (20, 21). Shh clearly induced *Pax1* expression in the micromass culture of wild-type presomitic mesoderm (Fig. 6E, left). In contrast, Shh-dependent expression of *Pax1* was totally abolished in the paraxial mesoderm derived from *Hipk1*$^{-/-}$ *Hipk2*$^{-/-}$ embryos (Fig. 6E, right), suggesting that Shh signaling to the *Pax1* induction was impaired. The expression of *Twist* was also reduced to about half that of the wild type. We did not see a significant reduction of *Pax1* expression in either single mutant (H. Koseki, unpublished). Therefore, it is likely that Hipk1 and Hipk2 are involved in the mediation of Shh-dependent proliferation of the paraxial mesoderm at least in part via transcriptional regulation of *Pax1* (6, 22).

Regulation of *Hox* gene expression by Hipks. HIPK1 and HIPK2 are capable of binding to the homeodomains of not only NK classes but also *Hox* cluster genes (37). Evidence for autoregulation of *Hoxa4* and *Drosophila Deformed* (4, 48) suggested the involvement of Hipks in the expression of *Hox* genes. This possibility was further supported by the following

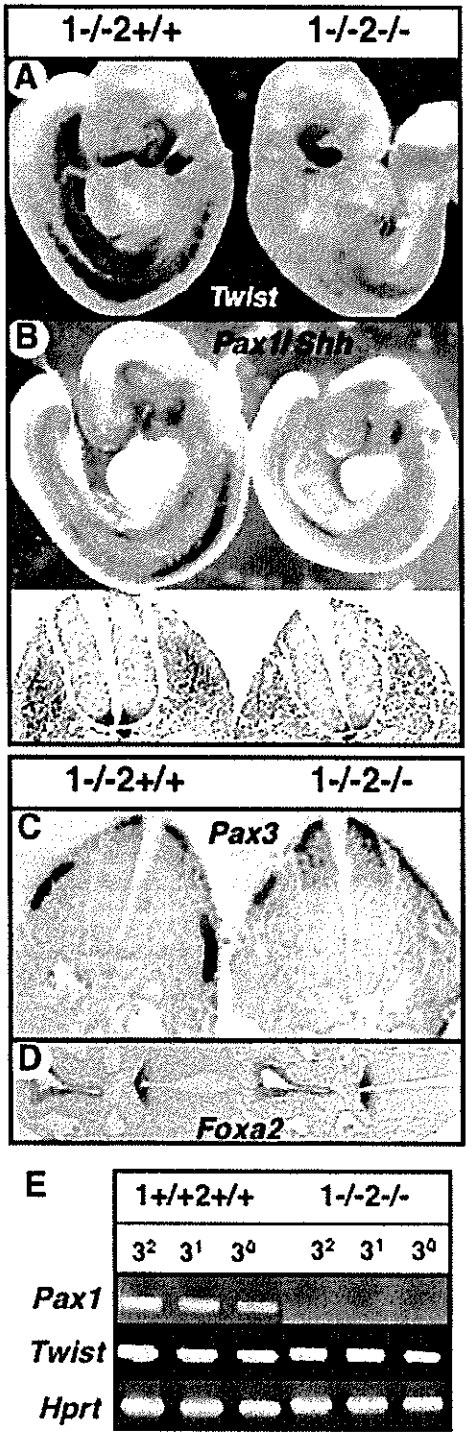

FIG. 6. Changes in Shh-dependent gene expression in the paraxial mesoderm and neural tube of *Hipk1*$^{-/-}$ *Hipk2*$^{-/-}$ embryos. (A) Expression of *Twist* in *Hipk1*$^{-/-}$ *Hipk2*$^{+/+}$ (left) and *Hipk1*$^{-/-}$ *Hipk2*$^{-/-}$ (right) embryos at 9.5 dpc. (B) Expression of *Pax1* and *Shh* in *Hipk1*$^{-/-}$ *Hipk2*$^{+/+}$ (left) and *Hipk1*$^{-/-}$ *Hipk2*$^{-/-}$ (right) embryos at 9.5 dpc. Whole-mount in situ hybridization (top) revealed significant reduction of Pax1 expression in *Hipk1*$^{-/-}$ *Hipk2*$^{-/-}$ (top right). Sections of the prospective cervical regions are shown (bottom). (C) Expression of *Pax3* in the prospective cervical regions of *Hipk1*$^{-/-}$ *Hipk2*$^{+/+}$ (left) and *Hipk1*$^{-/-}$ *Hipk2*$^{-/-}$ (right) embryos at 9.5 dpc. (D) Expression of *Foxa2* at the midgut level of *Hipk1*$^{-/-}$ *Hipk2*$^{+/+}$ (left) and *Hipk1*$^{-/-}$ *Hipk2*$^{-/-}$ (right) embryos at 9.5 dpc. (E) Impaired *Pax1* induction by Shh in explant culture of presomitic mesoderm from 9.5 dpc *Hipk1*$^{-/-}$ *Hipk2*$^{-/-}$ embryos. Total RNA extracted from the explant culture of presomitic mesoderm from wild-type (left) and *Hipk1*$^{-/-}$ *Hipk2*$^{-/-}$ (right) embryos were reverse transcribed and subjected to PCR for *Pax1* and *Twist*, with *hprt* used as a control.

observations. CRE-binding protein, which interacts with Hipk2, was shown to be involved in the regulation of *Hox* gene expression via binding to the *Hox* gene promoters (54). Furthermore, Hipk2 was demonstrated to be activated by Wnt signaling, which was also shown to impact *Hox* gene expression, in cultured cells (36, 41). Therefore, we examined the expression of *Hox* genes and the anterior-posterior specification of the axial skeleton in *Hipk* mutants. Sixty-nine and 20% of *Hipk1*$^{-/-}$ *Hipk2*$^{+/-}$ and *Hipk1*$^{+/-}$ *Hipk2*$^{-/-}$ mice, respectively, possessed ectopic ribs associated with the seventh cervical vertebra (C7) and missed the prominent spinous process from the second thoracic vertebra (T2), which may represent posterior transformations around the cervicothoracic boundary (Fig. 7A and B). The ectopic ribs were present in the single homozygotes with lower penetrance, whereas there were no changes in single heterozygotes (Fig. 7C). Therefore, Hipk1 and Hipk2 synergistically regulate the segmental identity. Next, we examined the *Hox* gene expression in the paraxial mesoderm and neural tube. In the paraxial mesoderm, no obvious changes were observed in *Hoxb6* or *Hoxb8* expression, which demarcates the prospective cervicothoracic boundary, in 11.5 dpc *Hipk1*$^{-/-}$ *Hipk2*$^{-/-}$ embryos (H. Koseki, unpublished). We went on to analyze the expression of *Hox* genes at 9.5 dpc, particularly in the neural tube. *Hoxb1* is predominantly expressed in rhombomere 4 (r4) and in the prospective spinal cord in the wild type (Fig. 7D). We found groups of *Hoxb1*-expressing cells in the r6 region in *Hipk1*$^{+/-}$ *Hipk2*$^{+/-}$ and *Hipk1*$^{-/-}$ *Hipk2*$^{-/-}$ embryos (Fig. 7E and F). The *Hoxb6* expression in the dorsal neural tube was seen up to the level of the fourth myotome in the wild type (Fig. 7G). This expression was extended to the level of the third myotome in *Hipk1*$^{-/-}$ *Hipk2*$^{-/-}$ embryos (Fig. 7H). In contrast, the expression of *Hoxa1*, *Hoxa2*, or *Hoxb3* was not changed in *Hipk1*$^{-/-}$ *Hipk2*$^{-/-}$ embryos (K. Isono, unpublished). Therefore, this suggests that Hipk1 and Hipk2 regulate the expression of a subset of *Hox* cluster genes during embryogenesis. It is possible that derepression of *Hox* expression in *Hipk* compound mutants may involve an interaction between Hox proteins and Hipk gene products. Otherwise, considering that Hipks act as repressors with histone deacetylase complexes (7, 37), Hipk1 and Hipk2 might regulate *Hox* expression at the transcription level. Whatever the intrinsic mechanisms that operate to maintain *Hox* gene expressions, *Hox* gene expressions are known to be regulated by various morphogenetic signals that include Wnts, retinoic acids, Notch signals, fibroblast growth factors, and maybe others (10, 41, 67). Derepression of *Hox* cluster genes in *Hipk* mutants might be another indication for the role of Hipks to integrate various signals and mediate appropriate cell growth to accomplish normal organ development.

The role of Hipks for activation of cell cycle checkpoints in embryonic cells. Previous studies using human tumor cell lines